Magnetic petrology of the Neoarchean granitoids in the Vila Jussara Suite, Carajás Province, Amazonian Craton

Luan Alexandre Martins de Sousa[1,2]* ⓘ, Roberto Dall'Agnol[1,2,3] ⓘ, Ingrid Roberta Viana da Cunha[1,2] ⓘ,
Fernando Fernandes da Silva[1,2] ⓘ, Davis Carvalho de Oliveira[1,2] ⓘ

Abstract

The Vila Jussara Suite (VJS) is formed by Neoarchean (~ 2.75 Ga) granites that are located in the Sapucaia Domain of the Carajás Province (CP), Amazonian Craton. Four petrographic varieties were identified in the VJS: biotite-hornblende monzogranite (BHMzG); biotite-hornblende tonalite (BHTnl); biotite monzogranite (BMzG); and hornblende-biotite granodiorite (HBGd). In terms of magnetic signature, BHMzG has two subgroups: the first subgroup has low magnetic susceptibility (MS) values (0.16×10^{-3} to 0.81×10^{-3}) and more commonly contains ilmenite with titanite rims; the second subgroup shows moderate to high MS (1.91×10^{-3} to 6.02×10^{-3}) and magnetite dominant over ilmenite. BHTnl has moderate MS (0.85×10^{-3} to 1.36×10^{-3}) and dominance of pyrite followed by magnetite. BMzG and HBGd have comparatively high MS (3.35×10^{-3} to 19.3×10^{-3} and 2.14×10^{-3} to 25.0×10^{-3}, respectively), with magnetite dominant over pyrite. The granite varieties of the VJS were formed under different oxygen fugacity ($fO2$) conditions, varying from reducing (< fayalite-magnetite-quartz (FMQ)) to oxidizing conditions (nickel-nickel oxide (NNO) to NNO+1). In addition, biotite-hornblende syenogranite occurs subordinately and shows high MS values and extremely high $FeO_t/(FeO_t + MgO)$ ratios, both in whole-rock and amphibole and biotite. The granites of the VJS are similar to other Neoarchean granites of the Carajás province. The reduced VJS granites are akin to the ferran granites of Planalto suite, Estrela Complex and Vila União area and the magnesian granites of VJS approach the magnesian granites of Vila União area.

KEYWORDS: Neoarchean; magnetic petrology; degree of oxidation; Carajás Province; ferroan and magnesian granitoids.

INTRODUCTION

The Archean terranes worldwide primarily consist of greenstone belt assemblages, associated with granitoids such as tonalite-trondhjemite-granodiorite (TTG), sanukitoids, leucogranodiorites, and leucogranites, with high Ba and Sr, and granites sensu stricto (Martin *et al.* 2005, Jayananda *et al.* 2006, Oliveira *et al.* 2011, Feio and Dall'Agnol 2012, Almeida *et al.* 2011, 2013, Dall'Agnol *et al.* 2017, Silva *et al.* 2018, Oliveira *et al.* 2018, Topno *et al.* 2018, Moyen and Laurent 2018, Rahaman *et al.* 2019, Chakraborti *et al.* 2019, Marangoanha *et al.* 2019).

[1]Programa de Graduação em Geologia e Geoquímica, Instituto de Geociências, Universidade Federal do Pará – Belém (PA), Brazil. E-mails: luansanmartins17@hotmail.com, robdal@ufpa.br, ingridvcunha@gmail.com, ffernandes@ufpa.br, davis@ufpa.br

[2]Granitoid Petrology Research Group, Instituto de Geociências, Universidade Federal do Pará – Belém (PA), Brazil.

[3]Instituto Tecnológico Vale – Belém (PA), Brazil.

*Corresponding author.

The VJS, which is the focus of this research, outcrops in the central and northern sections of the Sapucaia Domain of the CP and is part of the Neoarchean subalkaline magmatism (~2.75-2.73 Ga) of this province. Geochemically, it is composed of metaluminous to peraluminous granitoids with variable ferroan to magnesian character, as defined by Frost *et al.* (2001). These rocks show significant textural, mineralogical, and compositional heterogeneity and marked variations in oxygen fugacity (Dall'Agnol *et al.* 2017), which are reflected in their magnetic susceptibility (MS) values.

Magnetic petrology combines MS data with conventional petrology to establish relationships between the magnetic behavior of rocks and the characteristics of Fe-Ti oxide minerals (nature, composition, abundance, microstructure, and paragenesis) as well as the petrological parameters (Clark 1999). Various authors have applied magnetic petrology as an important tool for discussing magmatic processes, particularly the oxygen fugacity conditions under which granitic bodies formed and evolved, as well as the metallogenic specialization of granitoids (Czamanske and Mihalik 1972, Ishihara 1977, 1981, Frost 1991; Magalhães *et al.* 1994, Dall'Agnol *et al.* 1997, Geuna *et al.* 2008, Cunha *et al.* 2016, Oliveira *et al.* 2018, Salazar-Naranjo and Vlach 2018). In this study, magnetic petrology data on the granitoids of the VJS are presented and discussed to better understand the role of the degree of magma oxidation in the magmatic evolution of this suite and establish relationships between the magnetic behavior and the mineralogical, petrographic, and geochemical variations observed in this

suite. Lastly, this suite is compared with similar Neoarchean granitoids of the Amazonian Craton and of other cratons.

GEOLOGICAL CONTEXT

The CP is located in the southeastern section of the Amazonian Craton (Fig. 1A) and is considered the main Archean domain of the Central Amazonian Province (Tassinari and Macambira 2004) or an independent Archean province (Santos *et al.* 2006). Following the terms proposed by Santos *et al.* (2006), Vasquez *et al.* (2008) adopted the subdivision of the province into the Rio Maria and Carajás domains (CD), which are located, respectively, in southern and northern CP. More recently, Dall'Agnol *et al.* (2013) retained the Rio Maria Domain (RMD) and recognized three different domains in the north central portion of the CP, as follows (from south to north): Sapucaia Domain (SD), Canaã do Carajás Domain (CCD), and Carajás Basin (Fig. 1B).

The RMD was formed during the Mesoarchean (3.0 to 2.86 Ga; Macambira and Lancelot 1996, Althoff *et al.* 2000, Dall'Agnol *et al.* 2006, Oliveira *et al.* 2009, 2011, Almeida *et al.* 2011, 2013, Silva *et al.* 2018) and essentially consists of greenstone belts of the Andorinhas Supergroup (3.0 to 2.9 Ga) and different types of granitoids, including TGG rocks (2.98 to 2.93 Ga), sanukitoids, leucogranodiorites-granites with high Ba-Sr, and potassic leucogranites (2.87-2.86 Ga). Subsequently, these rocks were covered by sediments of the Rio Fresco Group (Docegeo 1988).

The SD (~2.95 to 2.73 Ga) is located in the central section of the CP and shows lithological similarities to the RMD, although it was affected by intense deformation during the Neoarchean and also includes rocks of the Neoarchean age. The main Mesoarchean units of the SD are as follows: greenstone belt of the Sapucaia Group formed by mafic-ultramafic metavolcanic rocks (Oliveira and Leonardos 1990, Souza *et al.* 2001); TTG suites of Caracol and Mariazinha tonalites (~2.93-2.91 Ga; Almeida *et al.* 2011) and Colorado trondhjemite (~2.93-2.85 Ga); São Carlos tonalite (~2.93 Ga), which is contrasted with the classic TTG suites (Silva *et al.* 2014); granitoids with high Mg of sanukitoid affinity (~2.87 Ga; Gabriel 2014); and leucogranodiorites enriched in Ba and Sr (~2.87 Ga, Nova Canadá leucogranodiorite, Leite-Santos and Oliveira 2016; and Pantanal leucogranodiorite, Teixeira *et al.* 2013). In the east central section of the SD, the Mesoarchean rocks are intersected by Neoarchean granitoid stocks of the VJS (2.75-2.73 Ga; D.C. Oliveira *et al.* 2010, P. A. Santos *et al.* 2013, Silva *et al.* 2010, 2014, 2020, Dall'Agnol *et al.* 2017; Fig. 1C).

The CCD is dominated by granites *sensu stricto* and charnockitic assemblages, which were intensely deformed during the Neoarchean. The Mesoarchean granitoids display varied geochemical signatures and ages (Moreto *et al.* 2011, Feio and Dall'Agnol 2012, Feio *et al.* 2013, Rodrigues *et al.* 2014). During the Neoarchean, the granites of the Planalto Suite and the granitoids of Vila União were formed along with the sodic granitoids of the Pedra Branca Suite, Pium diopside-norite, and charnockitic rocks (Huhn *et al.* 1999, Dall'Agnol *et al.* 2006, Feio *et al.* 2013, R. D. Santos *et al.* 2013, Cunha *et al.* 2016, Dall'Agnol *et al.* 2017, Oliveira *et al.* 2018, Marangoanha *et al.* 2019).

The Carajás Basin is located in the north section of the CP, and it predominantly consists of a sequence of metavolcano-sedimentary rocks of the Itacaiúnas Supergroup (Docegeo 1988, Machado *et al.* 1991, Vasquez *et al.* 2008, Martins *et al.* 2017). In addition, Neoarchean subalkaline granites occur frequently (Igarapé Gelado Granite, Barbosa 2004, Estrela Granite Complex, Barros *et al.* 2009, Serra do Rabo Granite, Sardinha *et al.* 2006).

In the Paleoproterozoic (~1.88-1.86 Ga), the Archean terranes of the CP were intersected by anorogenic granitic plutons and batholiths, and by associated mafic and felsic dike (Javier Rios *et al.* 1995, Mesquita *et al.* 2018, Dall'Agnol *et al.* 2005, Oliveira *et al.* 2008, Silva *et al.* 2016, Teixeira *et al.* 2017, 2018, 2019, Fig. 1C).

Geology of the Vila Jussara Suite

The VJS outcrops in the north and central sections of the SD and encompasses different granitic stocks (Fig. 2), which are intrusive in the São Carlos tonalite, Colorado trondhjemite, and Pantanal leucogranodiorite (Silva *et al.* 2014, Teixeira *et al.* 2013). The VJS bodies define a gently hilly terrain (Fig. 3A), have elongated shapes in the E-W direction, and are commonly associated with shear zones in the same direction. This suite consists of a set of heterogeneously deformed rocks showing penetrative foliations and commonly mylonitic textures, with kinematic markers suggesting sinistral transcurrent movements (Silva *et al.* 2020). The outcrops are usually shaped as meter-sized blocks (Fig. 3B).

The granitoids of the VJS are divided into four major petrographic groups: biotite-hornblende monzogranite (BHMzG), biotite monzogranite (BMzG), hornblende-biotite granodiorite (HBGd), and biotite-hornblende tonalite (BHTnl). The contact relationships between these varieties are transitional and usually imperceptible in the field. However, in some outcrops, porphyroclastic rocks of the HBGd group interspersed with BHTnl and BMzG are observed (Fig. 3C). Microgranular or mafic enclaves with elliptical shapes and centimetric to metric dimensions encompassed and partly digested by BHMzG are commonly found (Figs. 3D and 3E). Enclaves of tonalitic rocks are often hosted in the same BHMzG. Strong evidence of interactions between the magmas that form the BHTnl and BMzG varieties is observed, suggesting significant mingling processes (Dall'Agnol *et al.* 2017). These processes were studied by. Silva *et al.* (2020) and are outside the scope of the present study. In general, contacts between the VJS granitoids and host rocks are abrupt.

The spatial distribution of these petrographic facies is quite variable (Fig. 2). Zonal distribution and structuring are more evident in bodies of the central-west section (Fig. 2), whose structures, emplacement, and zoning were discussed in depth by Silva *et al.* (2020). One of those bodies, the northernmost of the three stocks in contact, shows central zones marked by the predominance of BHMzG and marginal zones that essentially consist of BMzG granites. In the pluton located to the southeast of this body, the available samples indicate the striking presence of the BMzG, HBGd, and BHTnl varieties, which show complex relationships and mingling features (Silva
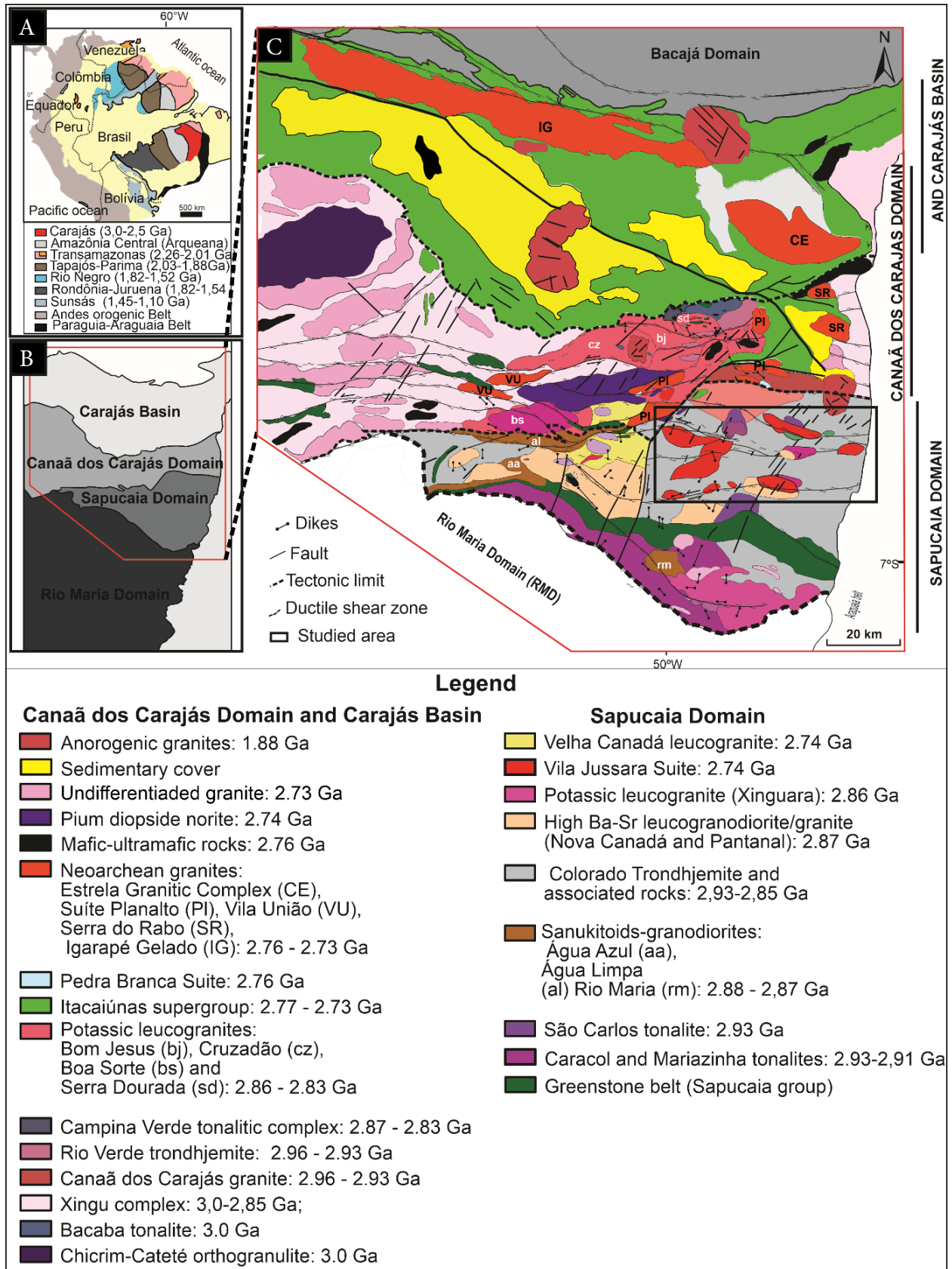
Figure 1. (A) Amazonian craton provinces (Santos *et al*. 2006); (B) tectonic domains of the Carajás Province (Dall'Agnol *et al*. 2013); (C) geological map of the central and northern sections of the Carajás Province (Vasquez *et al*. 2008, Almeida *et al*. 2011, Oliveira D.C. *et al*. 2010, Feio *et al*. 2013, Teixeira *et al*. 2013, 2017, Santos P.A. *et al*. 2013, Silva *et al*. 2014, Gabriel 2014, Rodrigues *et al*. 2014, Leite-Santos and Oliveira 2016, Marangoanha *et al*. 2019, modified).

et al. 2020). Lastly, the third southernmost body is dominated by BHMzG. In two other stocks, the first located in contact with the Pantanal leucogranodiorite and the second farther

to the east near the border between the Amazonian Craton and the Araguaia Belt (Fig. 2), only ferran granite varieties of BHMzG were described. Lastly, in the stock located in the
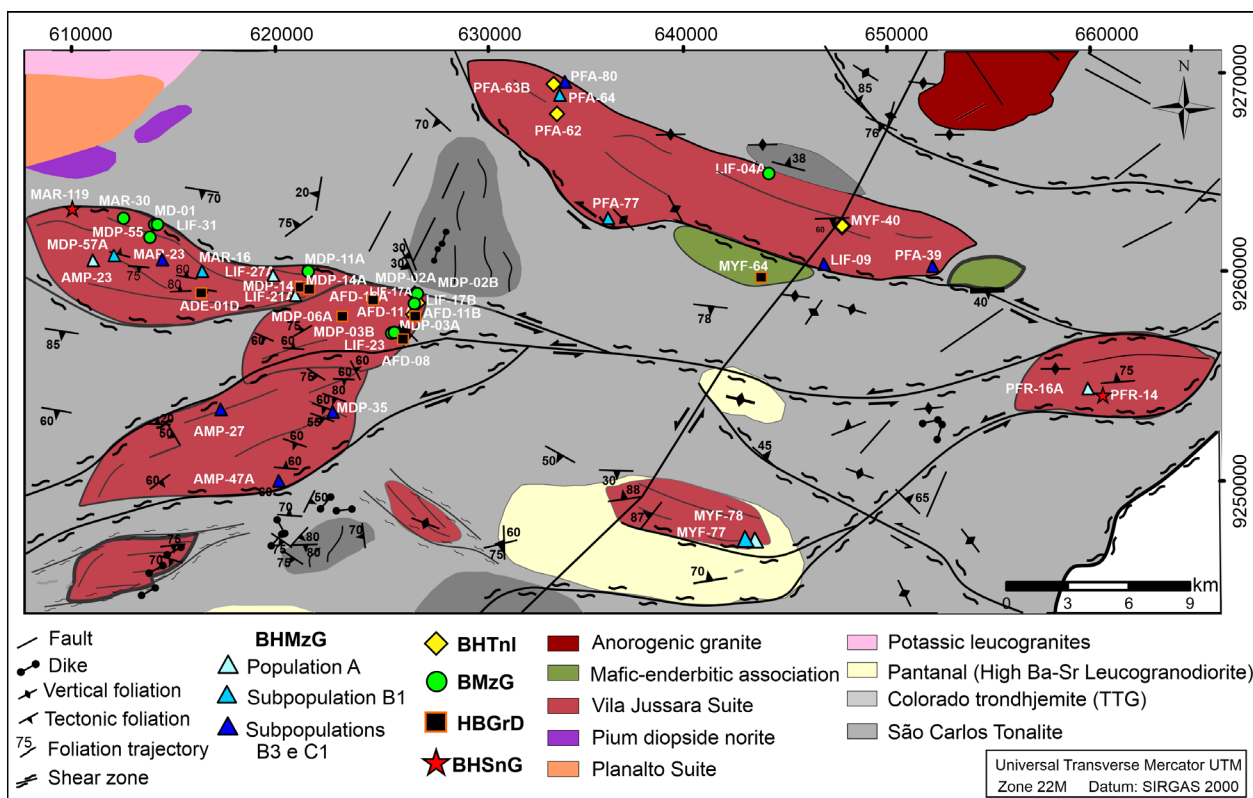
Figure 2. Simplified geological map (based on Silva *et al.* 2020 and Dall'Agnol *et al.* 2017, modified) highlighting the different granite bodies of the VJS and the location of the samples studied in detail in the present study.
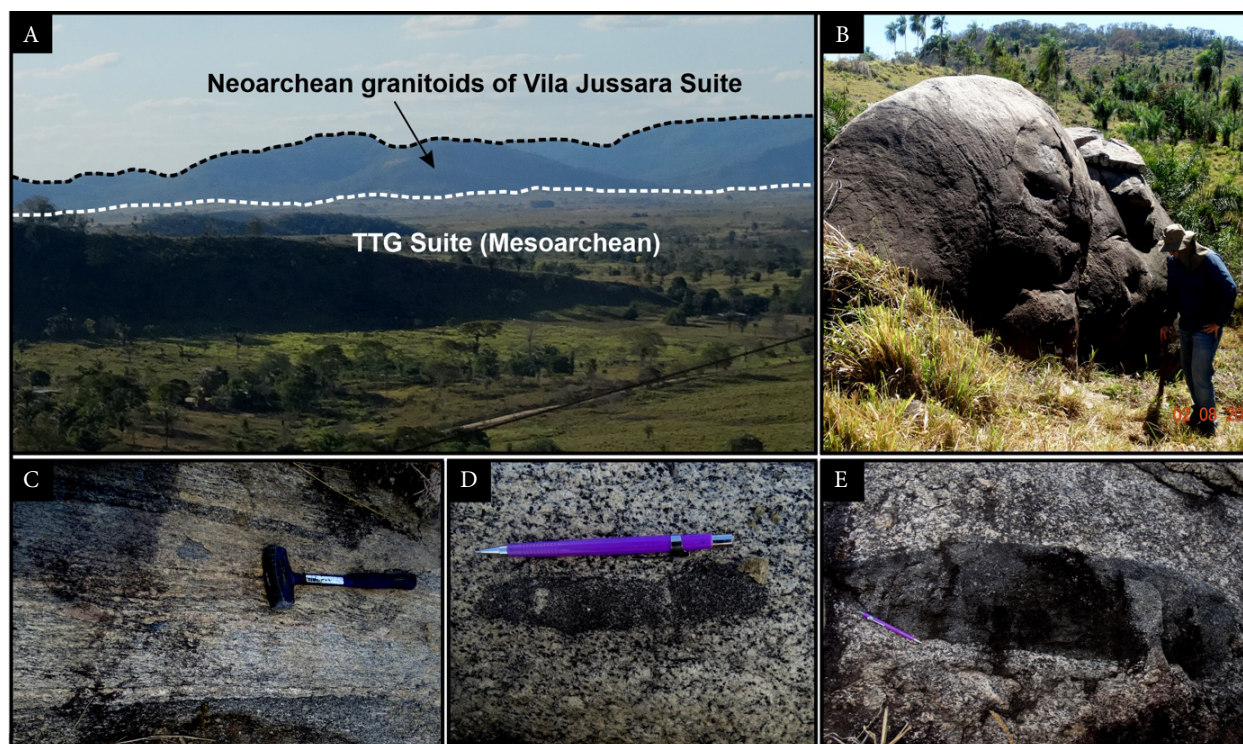
Figure 3. Field aspects of the VJS: (A) geomorphological aspect of the study granitoids, which define soft hills relative to the flattened morphological pattern of the host rocks; (B) main mode of occurrence in the form of metric blocks; (C) HBGd interspersed with rocks of tonalitic composition; (D) microgranular enclave partly digested by the host rock (BHMzG); (E) mafic microgranular enclave hosted in BHMzG.

north section of the SD, four varieties were described, indicating increased lithological diversity.

Geochronological dating by Pb evaporation in zircon and occasionally via sensitive high-resolution ion microprobe (SHRIMP) zircon U-Pb dating (Oliveira D.C. *et al.* 2010, Dall'Agnol *et al.* 2017) generally provide ages ranging from 2750 to 2730 Ma, although a slightly older age (2769 ± 10 Ma) was obtained in a tonalite sample from the northern body of the SD.

MATERIALS AND METHODS

Sampling and fieldwork

Sample locations in the granitoids from the VJS are shown in Fig. 2. All samples collected during the field-work weighed more than 5 kg each. Furthermore, samples collected on earlier occasions by institutional colleagues were also included in this study. Each sample is considered typical for the lithology of interest at the respective location. An overview of all samples assessed here is given in Tab. 1.

Petrography

Around 80 polished thin sections were studied and mineral modal contents in volume percent (vol%) were determined by counting a minimum of two thousand points per section in an orthogonal isometric grid, covering the entire specimen area in the thin section. Modal contents are collated in Tab. 2.

Optical petrography in transmitted light was used to identify locations suitable for in-situ assessment of mineral chemical composition (see below), with immaculate surface polish, free from inclusions, and with perpendicular mineral grain

Table 1. Sampling location, petrographic classification and magnetic susceptibility (MS) data of granitoids of the Vila Jussara Suite.

Sample	Petrographic varieties	MS average (×10⁻³SI)	Log MS	MS population	MS subpopulation	Longitude (UTM E)	Latitude (UTM N)
PFR-16A	Biotite-hornblende monzogranite	0.16	-3.80	A		661791	9253858
LIF-21A*	Biotite-hornblende monzogranite	0.18	-3.74	A		620906	9259083
AMP-23	Biotite-hornblende monzogranite	0.23	-3.64	A		620220	9260732
LIF-27A*	Biotite-hornblende monzogranite	0.31	-3.52	A		620017	9259925
MYF-77	Biotite-hornblende monzogranite	0.32	-3.49	B	B1	643178	9246812
PFA-64	Biotite-hornblende monzogranite	0.58	-3.24	B	B1	634424	9269740
MAR.16	Biotite-hornblende monzogranite	0.61	-3.21	B	B1	617081	9259994
MDP-57A	Biotite-hornblende monzogranite	0.77	-3.11	B	B1	612067	9261037
PFA-77	Biotite-hornblende monzogranite	0.81	-3.09	B	B1	636276	9262678
AMP-47A	Biotite-hornblende monzogranite	1.91	-2.72	B	B3	620137	9249906
LIF-26A*	Biotite-hornblende monzogranite	2.38	-2.62	B	B3	618163	9251275
LIF-25A*	Biotite-hornblende monzogranite	3.16	-2.50	B	B3	621456	9251047
MYF 78	Biotite-hornblende monzogranite	3.45	-2.46	B	B3	642932	9246810
LIF-09*	Biotite-hornblende monzogranite	3.62	-2.44	B	B3	647038	9260808
LIF-26B*	Biotite-hornblende monzogranite	3.70	-2.43	B	B3	618163	9251275
LIF-19*	Biotite-hornblende monzogranite	3.73	-2.43	B	B3	623648	9258116
MDP-44A	Biotite-hornblende monzogranite	4.29	-2.37	B	B3	611597	9250197
MDP-42A	Biotite-hornblende monzogranite	4.71	-2.33	B	B3	617106	9250595
PFA-80	Biotite-hornblende monzogranite	5.16	-2.29	B	B3	634312	9269358
MYF 64	Biotite-hornblende monzogranite	5.22	-2.29	B	B3	644065	9260038
AMP-27	Biotite-hornblende monzogranite	5.84	-2.23	C	C1	617346	9253574
PFA-78	Biotite-hornblende monzogranite	5.97	-2.22	C	C1	635839	9262776
PFA - 39	Biotite-hornblende monzogranite	6.02	-2.22	C	C1	651992	9261088
MAR.23	Biotite-hornblende monzogranite	6.02	-2.22	C	C1	614466	9260772
MAR.12	Biotite-hornblende monzogranite	6.20	-2.21	C	C1	611004	9263272
LIF-21B*	Biotite-hornblende monzogranite	7.29	-2.14	C	C1	620906	9259083
LIF-14C*	Biotite-hornblende monzogranite	8.27	-2.09	C	C1	624896	9258965
LIF-22*	Biotite-hornblende monzogranite	11.70	-1.93	C	C2	622864	9255398
LIF-23*	Biotite-hornblende monzogranite	18.00	-1.74	C	C2	622940	9254949
LIF-15*	Biotite-hornblende monzogranite	12.20	-1.91	C	C2	624495	9257993
LIF-17B*	Biotite-hornblende tonalite	0.85	-3.07	B	B2	626707	9258192
MDP-02E	Biotite-hornblende tonalite	0.86	-3.07	B	B2	626704	9258200
LIF-17E*	Biotite-hornblende tonalite	1.03	-2.99	B	B2	626707	9258192
PFA - 62	Biotite-hornblende tonalite	1.46	-2.92	B	B2	633710	9268486
MDP-02C	Biotite-hornblende tonalite	1.49	-2.91	B	B2	626704	9258200
PFA-63B	Biotite-hornblende tonalite	1.50	-2.88	B	B2	634077	9269740
AFD-11B	Biotite-hornblende tonalite	1.67	-2.87	B	B2	626622	9258168
LIF-17D*	Biotite-hornblende tonalite	1.88	-2.86	B	B2	626707	9258192
MYF-40	Biotite-hornblende tonalite	16.60	-1.78	C	C2	647586	9262500

Table 1. Continuation.

Sample	Petrographic varieties	MS average (×10⁻³)	Log MS (SI)	MS of population	MS of subpopulation	Longitude (UTM E)	Latitude (UTM N)
MDP-02B	Biotite monzogranite	3.37	-2.47	B	B3	626704	9258200
MDP-11A	Biotite monzogranite	4.22	-2.37	B	B3	619910	9259992
MDP-02A	Biotite monzogranite	5.00	-2.30	B	B3	626704	9258200
MD-01	Biotite monzogranite	5.75	-2.24	C	C1	614050	9262358
LIF-17A*	Biotite monzogranite	5.84	-2.23	C	C1	626707	9258192
LIF-24*	Biotite monzogranite	6.01	-2.22	C	C1	622986	9254124
LIF-18B*	Biotite monzogranite	6.32	-2.20	C	C1	626852	9258709
MDP-55	Biotite monzogranite	6.36	-2.20	C	C1	613843	9261885
LIF-30A*	Biotite monzogranite	7.46	-2.13	C	C1	616520	9260177
MAR.30	Biotite monzogranite	7.98	-2.10	C	C1	612555	9262904
LIF-13C*	Biotite monzogranite	8.50	-2.07	C	C1	625006	9259394
LIF-31*	Biotite monzogranite	8.76	-2.06	C	C1	614059	9262368
LIF-30B*	Biotite monzogranite	9.16	-2.04	C	C1	616520	9260177
MDP-12C	Biotite monzogranite	9.20	-2.04	C	C1	621613	9260243
LIF-04A*	Biotite monzogranite	10.40	-1.99	C	C2	645022	9265091
MDP-03A	Biotite monzogranite	10.50	-1.98	C	C2	626361	9257007
MDP-03B	Biotite monzogranite	12.60	-1.90	C	C2	626361	9257007
LIF-16A*	Biotite monzogranite	16.20	-1.80	C	C2	626361	9257010
MDP-14C	Biotite-hornblende granodiorite	2.14	-2.67	B	B3	621269	9259428
MDP-14E	Biotite-hornblende granodiorite	2.50	-2.60	B	B3	621269	9259428
PFA-63A	Biotite-hornblende granodiorite	2.53	-2.58	B	B3	634077	9269740
MDP-06A	Biotite-hornblende granodiorite	2.87	-2.54	B	B3	623648	9258136
MDP-14B	Biotite-hornblende granodiorite	3.45	-2.46	B	B3	621269	9259428
AFD-11A	Biotite-hornblende granodiorite	4.11	-2.39	B	B3	626622	9258168
MDP-36	Biotite-hornblende granodiorite	5.98	-2.22	C	C1	620941	9251856
LIF-29*	Biotite-hornblende granodiorite	7.22	-2.14	C	C1	620425	9260435
LIF-14A*	Biotite-hornblende granodiorite	7.53	-2.12	C	C1	624896	9258965
AFD-16A	Biotite-hornblende granodiorite	7.76	-2.11	C	C1	624791	9258906
LIF-17C*	Biotite-hornblende granodiorite	8.45	-2.07	C	C1	626707	9258192
MDP-12B	Biotite-hornblende granodiorite	8.71	-2.06	C	C1	621613	9260243
LIF-21D*	Biotite-hornblende granodiorite	8.88	-2.05	C	C1	620906	9259083
MDP-12A	Biotite-hornblende granodiorite	9.33	-2.03	C	C1	621613	9260243
LIF-16C*	Biotite-hornblende granodiorite	9.33	-2.03	C	C1	626361	9257010
LIF-13B*	Biotite-hornblende granodiorite	9.40	-2.03	C	C1	625006	9259394
MDP-42C	Biotite-hornblende granodiorite	9.85	-2.01	C	C2	617106	9250595
LIF-14B*	Biotite-hornblende granodiorite	10.50	-1.98	C	C2	624896	9258965
MDP-42B	Biotite-hornblende granodiorite	11.80	-1.93	C	C2	617106	9250595
MDP-02D	Biotite-hornblende granodiorite	12.30	-1.91	C	C2	626704	9258200
MDP-10	Biotite-hornblende granodiorite	13.10	-1.89	C	C2	621092	9257227
LIF-27D*	Biotite-hornblende granodiorite	13.80	-1.86	C	C2	620017	9259925
LIF-21C*	Biotite-hornblende granodiorite	14.10	-1.85	C	C2	620906	9259083
AFD-08	Biotite-hornblende granodiorite	14.20	-1.85	C	C2	626319	9256956
MDP-14A	Biotite-hornblende granodiorite	21.90	-1.66	C	C2	621269	9259428
MDP-11B	Biotite-hornblende granodiorite	25.00	-1.60	C	C2	619910	9259992
PFR-14	Biotite-hornblende syenogranite	9.56	-2.02	C	C1	662361	9253932
MAR.119	Biotite-hornblende syenogranite	30.10	-1.52	C	C2	610036	9263340

*Samples selected for the study recently collected; the remaining samples were borrowed from the institutional collection.

Table 2. Modal compositions of the granitoids of the Vila Jussara Suite.

Petrographic Varieties	Biotite-Hornblende monzogranite																Biotite-HornblendeTonalite					BHSnG	
Modal Classification	HBMzG	HBMzG	BHMzG	HBMzG	BHGd	BHMzG	BHGd	BHMzG	BHMzG	BHMzG	BHMzG	BHGd	BHGd	BHGd	BHGd	BHMzG	BHTnl	BHTnl	BHTnl	BHTnl	BHTnl	BHSnG	HBMzG
Magnetic Population	Population A				Subpopulation B1				Subpopulation B3					Subpopulation C1			Subpopulation B2					Subpopulation C1 and C2	
	PFR	AMP	LIF	MYF	PFA	MAR	MDP	PFA	AMP	LIF	LIF	PFA	MYF	PFA	PFA	MAR	MDP	PFA	MDP	AFD	MYF	PFR	MAR
Sample	16A	23	27A	77	64	16	57A	77	47A	9	26B	80	64	78	39	23	02E	62	02C	11B	40	14	119
Quartz	31.4	26.0	34.1	17.9	35.6	38.0	30.9	26.4	28.0	41.7	31.0	35.3	26.2	33.1	30.0	26.0	20.9	26.2	30.9	18.8	26.6	26.0	35.5
Plagioclase	32.2	30.0	22.9	35.1	32.9	22.9	39.9	32.5	25.0	20.1	20.0	26.9	34.5	31.0	43.0	30.0	38.4	46.3	30.0	44.4	54.3	32.6	13.2
Alkali-feldspar	25.0	23.0	26.9	32.6	12.1	25.8	18.1	26.2	24.0	23.2	24.4	12.0	11.4	11.0	9.0	23.0	2.1	1.2	6.8	0.0	1.3	28.1	45.2
Hornblende	4.9	8.1	8.1	3.6	12.0	7.2	11.8	9.8	11.8	7.1	15.1	11.7	18.5	12.2	7.4	12.8	26.3	15.2	13.5	10.3	8.7	3.4	2.1
Biotite	5.2	11.3	6.2	8.3	5.3	5.2	7.6	8.9	8.4	6.1	7.9	11.1	7.1	9.4	7.4	7.0	7.1	9.5	14.2	22.3	7.3	8.9	0.2
Titanite	0.6	0.7	1.4	1.0	-	0.4	1.4	1.2	1.9	0.7	1.1	1.2	0.3	-	1.7	0.8	3.4	0.3	2.9	1.5	0.2	-	0.1
Epidote	0.1	0.2	0.1	0.5	0.1	-	-	0.9	-	0.6	0.2	0.2	-	1.0	0.2	-	0.3	-	0.2	-	0.4	0.7	-
Zircon	0.2	-	0.1	0.2	0.1	-	0.1	0.1	-	0.1	-	0.3	-	0.1	-	0.1	0.2	-	0.4	-	-	0.1	0.1
Allanite	0.2	0.2	0.1	-	-	0.1	-	-	0.1	0.1	-	0.2	-	-	-	0.3	0.6	-	-	-	-	0.1	1.4
Apatite	-	0.2	-	-	0.1	-	-	-	0.4	-	-	0.2	0.3	-	-	-	-	-	-	-	0.2	0.0	-
Opaques	0.2	0.1	0.1	0.4	1.8	0.4	0.2	0.2	0.4	0.3	0.3	0.8	1.2	0.2	0.8	0.3	0.1	0.4	0.6	0.1	0.2	1.1	1.5
Mafic (M')	11.4	20.6	16.1	14.0	19.7	13.3	21.1	21.1	22.6	15.0	24.6	25.6	27.4	22.9	17.5	21.3	37.8	25.4	31.6	34.2	16.8	14.2	5.4
Felsic	88.6	79.2	83.9	85.6	80.6	86.7	88.9	85.1	77.4	85.0	75.4	74.4	72.1	75.1	82.0	79.0	61.4	73.7	67.7	63.2	82.4	86.7	93.9
Pl/A	1.3	1.3	0.9	1.1	20.8	0.9	2.2	1.2	1.0	0.9	0.8	2.2	3.0	2.8	4.8	1.3	18.7	38.6	4.4	44.4	41.8	1.2	0.3
A+Pl	57.2	53.0	49.8	67.7	45.0	48.7	58.0	58.7	49.0	43.3	44.4	38.9	45.9	42.0	52.0	53.0	40.5	47.5	36.8	44.4	55.6	60.7	58.4
*Quartz	35.4	32.9	40.7	20.9	44.2	43.8	34.8	31.0	36.4	49.1	41.1	47.5	36.3	44.1	36.6	32.9	34.1	35.5	45.6	29.7	32.4	30.0	37.8
*Alkali-feldspar	28.2	29.1	32.1	38.1	2.6	29.8	20.3	30.8	31.2	27.3	32.4	16.2	15.8	14.6	11.0	29.1	3.3	1.6	10.1	0.0	1.6	32.4	48.2
*Plagioclase	36.4	38.0	27.3	41.0	53.2	26.4	44.9	38.2	32.5	23.6	26.5	36.3	47.9	41.3	52.4	38.0	62.6	62.8	44.3	70.3	66.1	37.6	14.1
References	3	4	4	2	5	4	4	2	4	5	4	5	2	5	3	4	4	2	4	1	2	3	5

Table 2. Continuation.

Petrographic Varieties	Biotite monzogranite															Hornblende-biotite granodiorite										
Modal Classification	BGd	BGd	BMzG	BMzG	BMzG	BMzG	BGd	BMzG	BMzG	BMzG	BMzG	BMzG	BMzG	BMzG	BMzG	HBMzG	HBGd	HBGd	HBGd	HBGd	HBMzG	HBGd	HBGd	HBMzG	HBGd	HBGd
Magnetic Population	Subpopulation B3			Subpopulation C1					Subpopulation C2							Subpopulation B3			Subpopulation C1				Subpopulation C2			
	MDP	MDP	MDP	LIF	MD	LIF	MDP	MDP	LIF	MAR	LIF	LIF	LIF	MDP	LIF	MDP	MDP	MDP	AFD	AFD	MDP	MDP	AFD	MDP	ADE	MDP
Sample	02B	11A	02A	24	1	17A	18B	55	30A	30	13C	31	04A	03B	16A	14CII	14E	06A	16A	11A	12A	02D	8	14A	01D	02D
Quartz	33.1	29.9	35.2	36.1	24.1	31.6	34.9	31.3	29.9	33.9	28.6	30.6	33.7	28.2	29.8	31.4	28.1	27.5	26.7	28.6	32.6	29.5	30.6	26.8	29.8	29.5
Plagioclase	33.0	36.9	17.5	28.5	22.9	37.7	36.1	23.6	34.6	28.8	31.0	21.0	20.8	32.5	31.8	29.6	37.5	29.3	39.6	36.7	29.1	32.0	40.7	27.4	41.2	32
Alkali-feldspar	10.5	15.3	29.8	26.3	41.6	23.9	17.5	26.5	24.9	23.6	31.8	38.3	27.6	23.1	21.2	15.1	7.5	10.9	14.2	18.6	18.7	10.5	11.2	19.6	12.5	10.5
Hornblende	0.4	1.3	0.4	0.9	0.1	0.1	0.8	0.8	0.2	0.8	0.4	0.1	0.6	0.3	2.8	8.8	10.9	10.1	7.0	2.1	5.1	10.6	5.2	5.8	5.4	10.6
Biotite	17.8	14.0	13.2	8.1	8.4	5.8	10.1	13.9	8.4	10.6	6.5	8.6	11.7	11.9	11.9	13.4	13.5	17.4	10.2	10.1	11.5	13.0	9.3	16.5	9.0	13
Titanite	2.3	0.7	2.1	-	0.2	0.4	0.1	2.2	0.9	1.3	0.4	0.3	1.9	1.4	1.9	1.5	2.1	3.1	0.5	0.9	2.1	2.9	1.3	2.3	1.2	2.85
Epidote	0.1	0.4	0.3	0.1	0.2	0.2	0.3	0.1	0.3	-	0.7	0.6	2.2	0.4	0.1	-	0.2	0.1	0.9	0.9	0.4	0.2	0.1	0.1	0.4	0.15
Zircon	0.7	-	0.6	-	0.3	-	0.1	0.5	0.1	0.1	0.2	0.1	0.2	0.4	0.1	0.1	0.1	0.2	-	-	0.2	0.5	-	0.1	-	0.5
Allanite	0.5	0.1	0.2	-	0.2	-	0.1	0.4	0.1	-	0.2	-	0.2	0.3	-	-	0.1	0.3	-	-	-	0.4	-	-	0.2	0.35
Apatite	-	-	0.1	-	-	-	-	-	-	-	-	-	0.1	-	-	-	-	-	-	-	-	-	0.1	-	-	-
Opaques	0.8	0.3	0.7	0.1	0.2	0.3	0.1	0.7	0.4	0.9	0.2	0.4	1.1	0.6	0.4	0.2	0.1	0.3	0.7	0.6	0.4	0.8	0.8	1.3	0.6	0.75
Mafic (M')	22.5	16.8	17.4	9.2	9.6	6.8	11.5	18.4	10.5	13.7	8.6	10.1	17.8	15.0	17.2	24.0	26.9	31.5	19.3	14.6	19.6	28.1	16.7	26.1	16.8	28.1
Felsic	76.5	82.1	82.6	90.8	88.6	93.2	88.5	81.4	89.5	86.3	91.4	89.9	82.2	83.8	82.8	76.1	73.1	67.7	80.5	83.9	80.4	71.9	82.6	73.8	83.5	71.9
Pl/A	4.8	2.4	0.6	1.1	0.6	1.6	2.1	0.9	1.4	1.2	1.0	0.5	0.8	1.4	1.5	2.0	5.0	2.7	2.8	2.0	1.6	3.0	6.2	1.4	3.3	3.04
A+Pl	43.5	52.2	47.3	54.8	64.6	61.6	53.6	50.1	59.6	52.4	62.8	59.3	48.4	55.6	53.0	44.7	45.0	40.2	53.8	55.3	47.8	42.5	51.9	47.0	53.7	42.5
*Quartz	43.2	36.4	42.7	39.7	27.1	33.9	39.4	38.5	33.5	39.3	31.3	34.0	41.0	33.6	36.0	41.3	38.4	40.6	33.2	34.1	40.5	41.0	37.1	36.3	35.7	41
*Alkali-feldspar	9.7	18.7	36.1	28.9	47.0	25.6	19.8	32.6	27.9	27.3	34.8	42.6	33.6	27.6	25.6	19.8	10.3	16.1	17.6	22.2	23.3	14.6	8.7	26.6	15.0	14.6
*Plagioclase	47.1	44.9	21.2	31.4	26.0	40.5	40.8	29.0	38.7	33.4	33.9	23.3	25.4	38.8	38.4	38.9	51.3	43.3	49.2	43.7	36.2	44.4	54.2	37.1	49.3	44.4
References	4	4	4	4	4	4	4	4	4	4	4	4	5	4	4	4	4	4	1	4	4	4	4	4	4	4

Abbreviations: BHMzG = Biotite-hornblende monzogranite; Hornblende-biotite monzogranite; BMzG = Biotite monzogranite; BGd = Biotite granodiorite; BHMzG = Biotite-hornblende monzogranite; BHGd = Biotite-hornblende granodiorite; BHTnl = Biotite-hornblende tonalite; BHGd = Biotite-Hornblende granodiorite; BHSnG = Biotite-Hornblende Syenogranite; PI/A – plagioclase/alkali feldspar ratio; A + P – alkali feldspar + plagioclase sum; * – Qz, Afs, Pl, recalculated to 100%. Data source: [1]Silva (2012); [2]Teixeira (2013); [3]Santos (2013); [4]F.F Silva et al., 2020; [5] – this work.

boundaries. Mineral names in tables, micrographs, and figure legends are abbreviated according to Whitney and Evans (2010).

Scanning electron microscopy

Before SEM assessment, the surface of polished sections was made electrically conductive with ~20 nm carbon in a Quorum Q150T-ES sputtering device to minimize charging in SEM or electron probe micro-analysis (EPMA). Fe-Ti oxide minerals and local assemblages were identified in a Zeiss Sigma VP SEM instrument equipped with an IXRF Sedona SD energy-dispersive (X-ray) spectrometer (EDS), operated at < 10^{-5} Torr, constant 8.5 mm working distance, accelerating voltage 20 kV, beam current of 500 pA (measured on Faraday cup), with beam diameter set to 1 μm, and counting time 30 s with EDS detector dead time < 20%. Observations by SEM and semi-quantitative analyses by EDS were used to prepare for mineral chemistry.

Mineral chemistry by electron probe micro-analysis

For quantitative chemical analysis of amphibole and biotite compositions, carbon-coated polished thin sections were analyzed in a JEOL JXA8230 EPMA instrument located at Universidade Federal do Pará Institute of Geosciences (IG-UFPA), equipped with five wavelength-dispersive spectrometers (WDS) and one EDS. The instrument was operated in high vacuum (<$5x10^6$ Torr), at 15kV accelerating voltage, 20 nA beam current (on Faraday cup), beam diameter set to 1 μm for non-silicates, defocused to 10 μm for hydrous silicates to minimize element (Na, K, Al, Si) migration (see Morgan and London 2005). Na and F were allocated to be measured on WDS first in each analytical run, and all elements were measured on their respective Kα lines, 30 s on peak and 10 s each on low and high backgrounds. The EPMA instrument was internally calibrated against natural and synthetic mineral standards: andradite (Si, Ca), microcline (Al, K), hematite (Fe), olivine (Mg), albite (Na), pyrophanite (Ti, Mn), vanadinite (V, Cl), and topaz (F). Raw element data were corrected using the CITZAF algorithm of Armstrong (1995), as implemented in the JEOL proprietary instrument software, and corrected element contents were converted to oxides assuming stoichiometry. Net lower limits of detection (LLD) are listed per element, together with the data.

Element oxide contents in weight percent (wt%) were recast into mineral composition formulae in atoms per formula unit (apfu) using guidelines from Papike (1987, 1988), and the appendices in Deer *et al.* (2013). Amphibole compositions were classified according to Hawthorne *et al.* (2012) and mica compositions according to Rieder *et al.* (1998). The Fe^{+3}/Fe^{+2} ratios in amphibole were estimated based on charge balancing (Schumacher 1997). Selected results are collated in Tabs. 4 and 5. Processed composition data were plotted using the GDCkit freeware of Janoušek *et al.* (2006).

Magnetic susceptibility

Magnetic susceptibilities of whole-rock samples (Tab. 1) were determined using a ZH Instruments SM-30 shirt-pocket susceptibility meter, located at the Laboratory of Magnetic Petrology (IG-UFPA), capable of measuring susceptibilities as low as $1x10^{-7}$ (in SI units). Each rock sample was measured on three flat faces. The arithmetic mean values for each sample were statistically assessed with Minitab 17 freeware. Data are plotted on a logarithmic scale.

RESULTS

Petrography of the Vila Jussara Suite

Modal composition and petrographic classification

The modal composition data presented here were supplied with literature data from Silva (2012), Teixeira (2013), Santos (2013), and Silva *et al.* (2020), plus some additional data obtained by the authors (Tab. 2).

The granitoids of the VJS are rose to whitish gray, medium to coarse grained, anisotropic, leucocratic rocks (M1 varying between 5.4 to 34.2 vol %, except for one tonalite sample; Tab. 2). The rocks of this suite have variable proportions of alkali feldspar and plagioclase. The main mafic phases are amphibole and biotite, which usually occur associated in variable proportions, except for the BMzG which contains little or no amphibole. Accessory minerals include titanite, epidote, allanite, zircon, apatite, ilmenite, magnetite, and pyrite.

Their modal compositions were plotted in Q-A-P and Q-(A+P)-M' diagrams (Le Maitre *et al.* 2002; Fig. 4, Tab. 2). Four main rock varieties were distinguished:

- biotite-hornblende monzogranite with subordinate granodiorite (BHMzG);
- biotite-hornblende tonalite with rare occurrences of equigranular granodiorite (BHTnl);
- biotite monzogranite with rare occurrences of granodiorite (BMzG);
- hornblende-biotite granodiorite with rare occurrences of monzogranite (HBGd).

In addition to these, a biotite-hornblende syenogranite to monzogranite (BHSnG) shows specific characteristics that prevent its inclusion in the previous groups. A synthesis of the main petrographic and magnetic petrology data of these four varieties is shown in Tab. 3.

The BHMzG was subdivided into two subgroups: the first subgroup corresponds to the reduced ferroan BHMzG and the second subgroup is composed of the oxidized ferroan BHMzG. The mafic and opaque modal contents are usually higher in the oxidized ferroan BHMzG compared to the reduced ferroan BHMzG (Tab. 3, Fig. 4). Ilmenite is the dominant opaque mineral in subgroup 1, whereas magnetite with subordinate pyrite and ilmenite is the main opaque phase in subgroup 2. The lowest magnetic values of the VJS are registered in the reduced BHMzG and increase substantially in the oxidized BHMzG (Tab. 3).

The HBGd variety has, in general, higher modal contents of mafic minerals compared to the BMzG samples (Tab. 3, Fig. 4). These varieties show moderate to high values of MS, and their
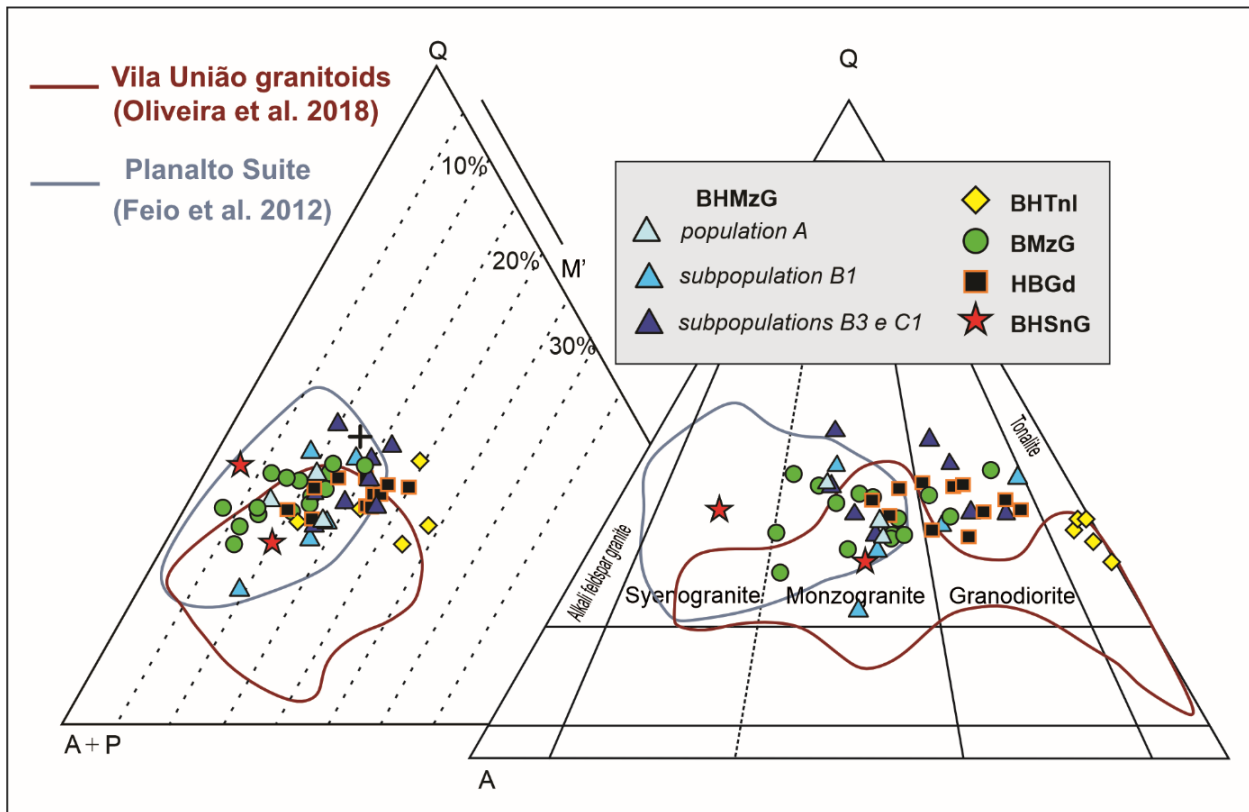
Figure 4. Q-A-P and Q-(A+P)-M' modal diagrams for granitoids of the VJS (fields according to Le Maitre *et al.* 2002). Modal data were obtained by the authors or compiled from previous studies by the GPPG (*cf.* Tab. 2).

main phase among Fe-Ti oxide minerals is magnetite. The BHTnl variety has the highest content of mafic minerals of the whole suite (Tab. 3, Fig. 4). These rocks have relatively moderate values of MS, and the main opaque phase corresponds to pyrite, except for sample MYF-40, which has a high MS value and magnetite as the dominant opaque mineral phase. Lastly, the BHSnG samples display variable modal contents of mafic minerals, high magnetite content, and also high MS values (Tab. 3).

Microstructure and texture/fabric

The rocks studied show penetrative foliation marked by the preferential orientation of ferromagnesian minerals and deformed feldspars and quartz. The BHMzG variety has an inequigranular texture, medium to coarse grain size. Some rocks still preserve features of hypidiomorphic granular texture; however, protomylonites and mylonites are found (Fig. 5A). In general, the BMzG and HBGd are porphyroclastic rocks with medium to coarse phenocrysts (Figs. 5D and 5G). In the BMzG, porphyroclasts are mostly alkaline feldspar (Figs. 5D and 5E), and in the HBGd, plagioclase porphyroclasts are more common (Figs. 5G and 5H). In both varieties, the matrix essentially consists of quartz-feldspar aggregates derived from recrystallization. The mafic minerals form aggregates and show fine to medium grain size (Figs. 5F and 5I). In addition, the HBGd has a higher matrix-to-porphyroclast ratio (Figs. 5G and 5H). Biotite-hornblende tonalites usually have medium grain size and hypidiomorphic granular texture and are less recrystallized than the rocks from the previous groups (Figs. 5J and 5L).

The microstructural aspects of the VJS were discussed in more detail by Silva *et al.* (2020).

Quartz: some fine to medium grain size (0.2-3 mm) subhedral to anhedral crystals preserve partly igneous textures. In addition, the most deformed grains occur in three morphological types:

- in ribbons with fine grain size (< 1 mm) and moderate undulose extinction;
- in polycrystalline aggregates composing the matrix or forming fine grain size (< 1 mm) anhedral subgrains of recrystallized crystals, which show moderate undulose extinction and polygonal contacts with each other (Figs. 5B, 5E and 5H);
- in fine anhedral grains included in potassium feldspar crystals.

Alkaline feldspar crystals occur in two petrographic types: in porphyroclasts with albite-pericline twinning and in new grains and subgrains forming the matrix. Although the phenocrysts were originally subhedral with coarse grain size (> 5 mm), their original shape was usually obliterated, with the crystals displaying oval shape and xenomorphic contours. The crystals of the recrystallized matrix form fine- to very-fine-grained polycrystalline aggregates and are associated with quartz, with which they present lobed contacts (Fig. 5E).

Plagioclase occurs in two petrographic types: subhedral phenocrysts or porphyroclasts with medium to coarse grain size (Fig. 5L), and albite and albite-Carlsbad polysynthetic twinning, which show irregular contacts with each other and with other minerals and usually display alteration to white

Table 3. Synthesis of petrographic, magnetic susceptibility, whole rock, amphibole, and biotite chemical data of the VJS.

Variety	Subgroup/SM Population	Petrographic Classification	Mafic modal content wt%	Modal opaques Vol%	Opaque phases	Magnetic Susceptibility SI	Log Magnetic Susceptibility	(FeO/(FeO + MgO) in Whole rock	Fe/(Fe + Mg) in amphibole	Fe/(Fe + Mg) in biotite
BHMzG - Group 1	reduced ferroan / A	BHMzG	11.5 - 20.6	0.1-0.11	Ilm	0.16×10^{-3} to 0.31×10^{-3}	-3.80 to -3.52	0.90 - 0.95	0.90 - 0.91	0.85 - 0.88
	reduced ferroan / B1	BHMzG (BHGd)	13.3 - 21.1	0.2-0.4 (1.2)	Ilm (Mag)	0.32×10^{-3} to 0.81×10^{-3}	-3.49 to -3.09	0.84 - 0.95	0.82 - 0.85	0.77 - 0.81
BHMzG - Group 2	oxidized ferroan / B3	BHMzG (BHGd)	15.0 - 27.4	0.22-1.2	Mag (Py-Ilm)	1.91×10^{-3} to 5.22×10^{-3}	-2.72 to -2.29	0.84 - 0.87	xx	xx
	oxidized ferroan / C1	BHMzG (BHGd)	17.5 - 22.9	0.28-0.80	Mag (Py-Ilm)	5.84×10^{-3} to 18.0×10^{-3}	-2.23 to -1.74	0.85 - 0.89	0.73 - 0.77	0.65 - 0.67
BHTnl	magnesian / B2	BHTnl (BHGd)	25.4-37.8	0.2-0.6 (1.1)	Py-Mag (Ilm)	0.85×10^{-3} to 1.36×10^{-3}	-3.07 to -2.86	0.75 - 0.76 (0.85)	0.68-0.73/0.58-0.63	0.67 - 0.7
	magnesian / C2	BHTnl	16.8	0.5	Mag (Py-Ilm)	16.6×10^{-3}	-1.78	0.76	0.49 - 0.51	0.52 - 0.55
	magnesian / B3	BMzG (BGd)	16.8 - 22.5	0.3-0.8	Mag (Py)	3.35×10^{-3} to 6.01×10^{-3}	-2.47 to -2.25	0.79	xx	xx
BMzG	magnesian / C1	BMzG	6.8-18.4	0.1 - 0.9	Mag (Py)	6.32×10^{-3} to 9.20×10^{-3}	-2.24 to -2.06	0.79 - 0.81	0.63 - 0.66	0.53 - 0.56
	magnesian / C2	BMzG	15.0 - 17.8	0.4 - 1.1	Mag (Py-Ilm)	10.04×10^{-3} to 19.3×10^{-3}	-1.99 to -1.80	0.78 - 0.8	0.61 - 0.62	0.52 - 0.55
	magnesian / B3	HBGd	24.0 - 31.5	0.1 - 0.3	Mag-Py (Ilm)	2.14×10^{-3} to 6.01×10^{-3}	-2.67 to -2.25	0.78	xx	0.64 - 0.65
HBGd	magnesian / C1	HBGd (HBMzG)	14.6 - 19.6	0.4 - 0.7	Mag-Py	6.02×10^{-3} to 9.33×10^{-3}	-2.22 to -2.03	0.76 - 0.81	0.60 - 0.70	0.57 - 0.62
	magnesian / C2	HBGd	16.7 - 28.1	0.6 - 1.3	Mag-Py	11.8×10^{-3} to 25.0×10^{-3}	-1.93 to -1.60	0.8 - 0.83	0.60 - 0.68	0.56 - 0.58
BHSnG	reduced / C1 - C2	HBSnG (HBMzG)	5.4 - 14.2	1.1 - 1.5	Mag	12.17×10^{-3} - 30.1×10^{-3}	-2.02 / -1.52	0.94 - 0.99	0.93 - 0.95	xx

Abbreviations (according to Whitney and Evans 2010): Ilm: ilmenite; Mag: magnetite; Py: Pyrite; BHMzG: Biotite-hornblende monzogranite; BHGd: Biotite-hornblende granodiorite; BHTnl: Biotite-hornblende tonalite; BMzG: Biotite monzogranite; HBGd: Hornblende-biotite granodiorite; HBMzG: Hornblende-biotite monzogranite; BHSnG: Biotite-hornblende syenogranite.
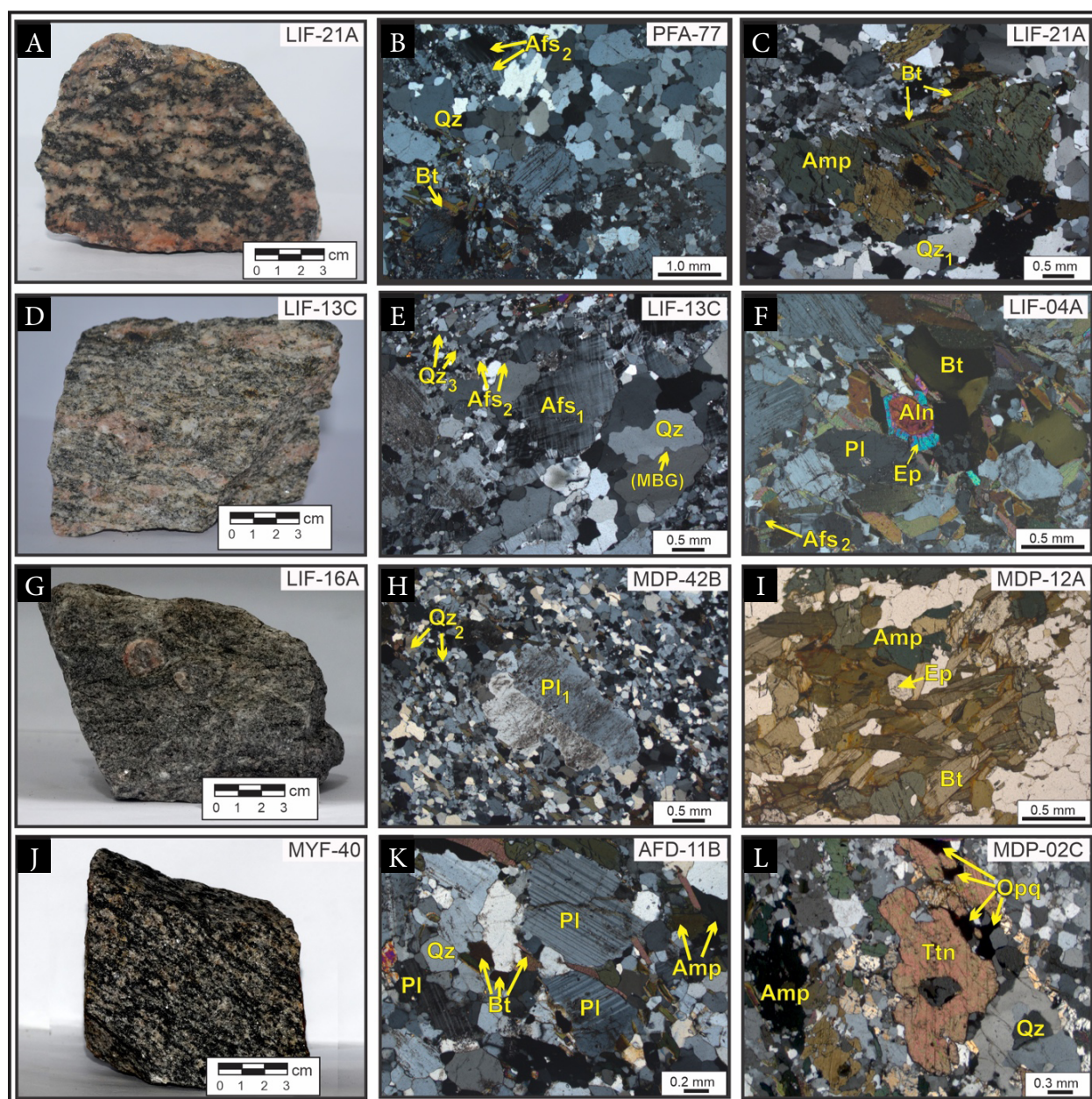
Figure 5. (A) Macroscopic aspect of BHMzG; (B) quartz subgrains forming the matrix in BHMzG; (C) amphibole crystals partly replaced by biotite in BHMzG; (D) macroscopic aspect of BMzG with porphyroclastic texture; (E) macroscopic aspect of BMzG showing fine quartz crystals with grain boundary migration; (F) allanite euhedral crystal bordered by an epidote rim associated with biotite in BMzG; (G) macroscopic aspect of HBGd; (H) plagioclase porphyroclast in quartz-feldspar matrix derived from recrystallization in HBGd; (I) amphibole and biotite crystals associated with euhedral magmatic epidote, forming a mafic aggregate; (J) macroscopic aspect of equigranular BHTnl; (K) hypidiomorphic granular texture in BHTnl; (L) subhedral titanite crystals exhibiting irregular contacts with opaque minerals in BHTnl. (B, C, E, F, H, K, and L) photomicrographs in polarized light from an optical microscope, with flat polarized light in panel i and cross-polarized light in all others.

mica in their nuclei; fine grains that form the recrystallized matrix of the rock.

Amphibole occurs as subhedral to euhedral crystals of medium to fine grain size (0.3-3 mm) that are commonly oriented (Fig. 5C) and assembled with biotite, titanite, epidote, and Fe-Ti oxide minerals, thus forming mafic clusters. Contours and contacts with biotite are sometimes straight and, with other minerals, irregular (Fig. 5I). According to EPMA data, the amphibole composition ranges from hastingite to its transition to magnesio-hastingsite.

Biotite crystals are sub- to anhedral with sizes ranging from 0.2 to 2.5 mm, and they show serrated terminations and pleochroism ranging from pale yellow to dark brown. The contacts are irregular or sometimes rectilinear to each other and to plagioclase, quartz, epidote, and amphibole crystals (Fig. 5F). In general, these crystals are oriented and surround the alkaline feldspar phenocrysts. Biotite has a ferroan composition that approaches an annite composition in the most iron-rich terms (EPMA data).

Titanite predominantly occurs as sub- to anhedral crystals that are locally euhedral, of fine grain size, and usually associated with mafic aggregates (Fig. 5L). It also occurs associated with Fe-Ti oxide minerals, typically forming rims involving ilmenite crystals, which it partly replaces.

Epidote occurs as euhedral to subhedral crystals of fine grain size, and it is usually associated with mafic aggregates and shows rectilinear contacts with biotite (Fig. 5I) and irregular contacts with the other minerals. Epidote commonly forms rims around metamict allanite cores (Fig. 5F). Epidote was interpreted as being of magmatic origin by Dall'Agnol *et al.* (2017) and Cunha *et al.* (2021) based on textural and compositional criteria.

Apatite occurs as fine-grained prismatic crystals that are generally included in alkaline feldspar crystals or associated with mafic aggregates. *Zircon* occurs as euhedral to subhedral crystals of fine grain size.

Opaque minerals form sub- to anhedral or locally euhedral crystals of fine grain size and are usually associated with mafic minerals. These minerals will be described in detail in the next section.

Magnetic susceptibility and opaque mineral assemblages

Magnetic susceptibility

MS data on the VJS were recorded in samples from different bodies and collected from different areas; therefore, they do not represent the evolution of a single magma. The MS values measured in samples from the VJS are listed in Table 1 and summarized in Tab. 3. They ranged from 0.16×10^{-3} to 30.13×10^{-3} with a median of 5.48×10^{-3} (SI) and are distributed from -3.80 to -1.52 (log SI) (Fig. 6, Tab. 1). The normal probability plot of the rocks studied distinguished three magnetic populations termed populations A, B, and C (Fig. 6A). In these populations, the MS values ranged, respectively, from 0.16×10^{-3} to 0.32×10^{-3} (log -3.80 to -3.52. SI), from 0.32×10^{-3} to 6.01×10^{-3} SI (log -3.49 to -2.25) and from 6.02×10^{-3} to 30.13×10^{-3} SI (-2.24 to -1.52). Populations A, B, and C account for 11vol%, 50.6vol%, and 38.4vol% of all study samples, respectively (Tab. 1). The frequency histogram revealed a bimodal pattern of MS measurements in the rocks of the suite (Fig. 6B).

The four main rock varieties of the suite were distributed in one or more MS populations, thus defining different MS subgroups. All subgroups are shown in an integrated probability plot and histograms specific to each rock variety of the suite (Fig. 7).

Petrographic texture/fabric associated with magnetic susceptibility

Biotite-hornblende monzogranite

This variety shows a wide variation in MS and is distributed in the three populations (Figs. 7A, 7B and 7C). It was subdivided into two subgroups, with the first formed by samples with low MS of population A and subpopulation B_1 and the second formed by samples with higher MS values of subpopulations B_3 and C_1 (Tabs. 1 and 3, Fig. 7C).

Subgroup 1 encompasses all samples from population A and is characterized by the occurrence of ilmenite with titanite rims (Figs. 8A and 8B), the absence of magnetite, and low modal content of opaque minerals (usually 0.10vol%; Tab. 3).
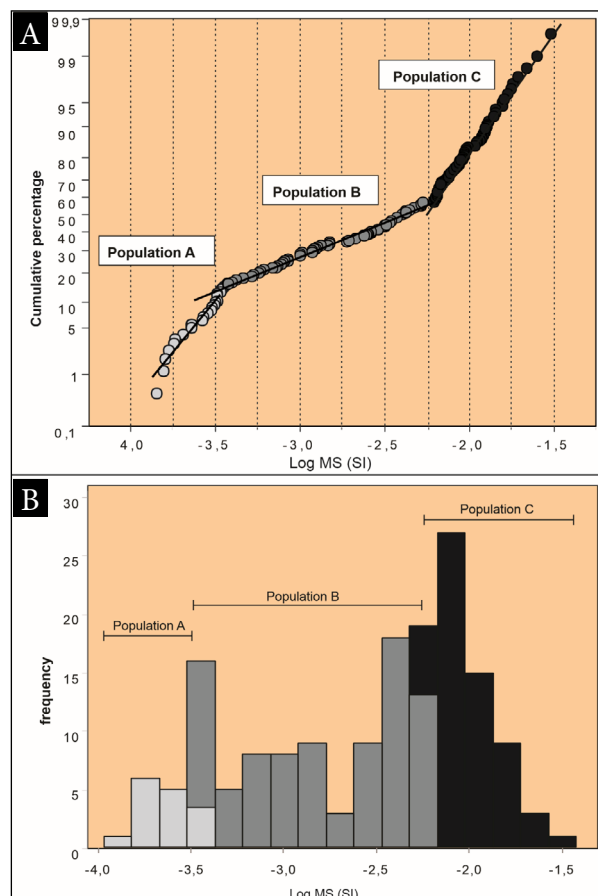

Figure 6. (A) Probability plot of study rocks indicating the existence of three magnetic populations; (B) MS histogram of the set of samples from VJS showing a bimodal distribution.

In addition, *subgroup 1* consists of samples from subpopulation B_1 that present ilmenite with titanite rims as the most abundant opaque mineral as well as crystals of magnetite and, occasionally, pyrite partially replaced by goethite (Fig. 8C, Tab. 3).

In subgroup 2, magnetite is the most abundant opaque mineral (Fig. 8D, Tab. 3), followed by pyrite (± chalcopyrite), which is partly or totally transformed into goethite, and by ilmenite crystals with fine hematite exsolution lamellae associated with titanite. The magnetite generally reveals mild to moderate alteration to martite.

In samples of subgroup 1, ilmenite crystals show similar textural aspects in populations A and B_1 and are found as fine, individual crystals (Ilm I; see e.g. Haggerty 1991, Dall'Agnol *et al.* 1997) that are usually surrounded by titanite rims (Figs. 8A and 8B) and commonly associated and included in biotite and amphibole crystals. In the samples of subpopulation B_1, ilmenite is also dominant and magnetite occurs as fine subhedral crystals associated with pyrite (± chalcopyrite) (Fig. 8C). Conversely, in samples from subgroup 2, magnetite is dominant and forms subhedral crystals (Fig. 8D). Pyrite crystals had a fine grain size and euhedral to subhedral character and mostly showed intense alteration to goethite.

Biotite-hornblende tonalite

This variety has moderate modal contents of opaque minerals and is concentrated in population B (subpopulation B_2; Figs. 7A, 7B and 7D), except for sample MYF-40 of
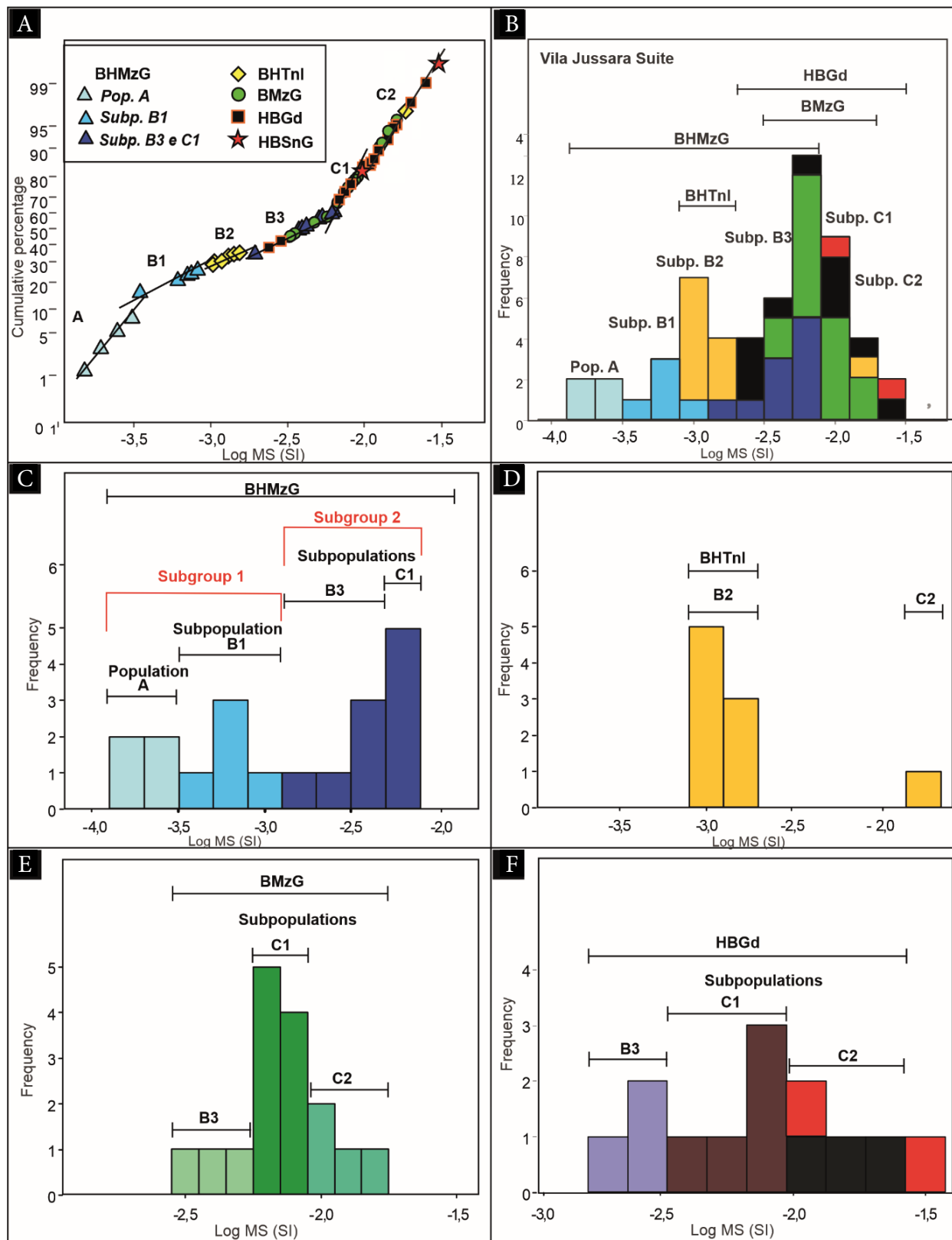
Figure 7. (A) Integrated probability plot of all VJS samples showing the distribution of established varieties and subgroups; (B) integrated MS frequency histogram of study rocks highlighting the main petrographic groups and the distribution of their samples in different populations as defined in the probability plot; frequency histograms of: (C) the biotite-hornblende monzogranite (BHMzG) variety; (D) the biotite-hornblende tonalite (BHTnl) variety; (E) the biotite monzogranite (BMzG) variety; (F) the hornblende-biotite granodiorite (HBGd) variety, including samples of BHSnG granites (red).

subpopulation C_2 (Tab. 3). In this variety, sulfides (pyrite ± chalcopyrite) generally dominate over magnetite and ilmenite is scarce (Tab. 3). Ilmenite crystals are similar to those observed in subgroup 1 of BHMzG, despite usually showing hematite

exsolution lamellae, as well as zones where hematite dominates and includes ilmenite lamellae (Fig. 9A). Sulfides are more abundant in this group than in subgroup 2 of BHMzG (Tab. 3). Pyrite always widely dominates over chalcopyrite and occurs
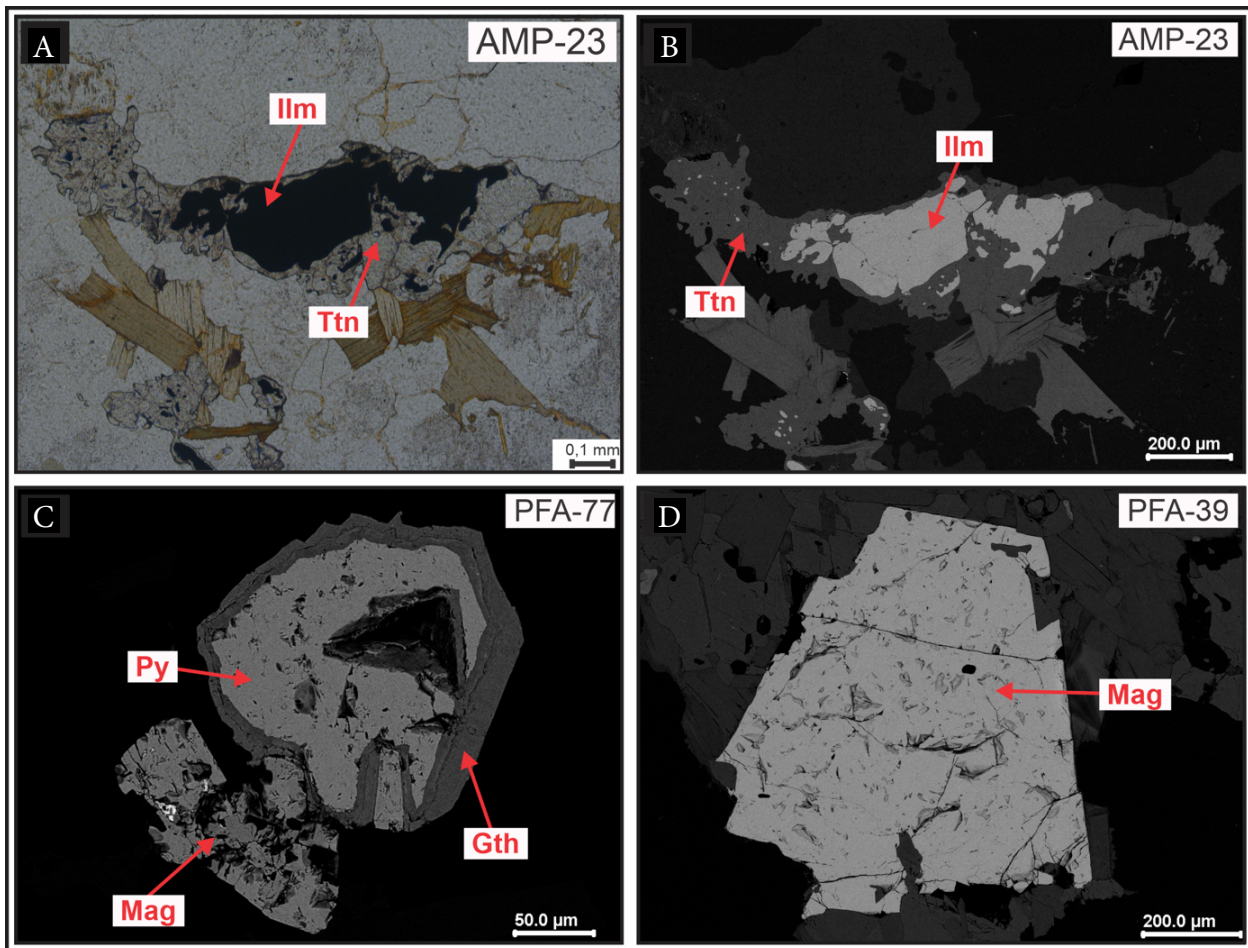
Figure 8. Textural aspects of representative samples of Fe and Ti oxide minerals of biotite-hornblende monzogranite: (A and B) ilmenite with titanite rim associated with biotite; sample from subgroup 1, population A; (C) originally euhedral pyrite crystal partly altered to goethite, which is associated with subhedral magnetite; subgroup 1, subpopulation B_1; (D) subhedral magnetite crystal; sample from subgroup 2, subpopulation C_1. A: flat polarized light photomicrograph; B, C, D: backscattered electron images acquired under SEM. b: same section shown in A.

as euhedral to subhedral crystals partly or entirely altered to goethite, generating goethite pseudomorphs. Magnetite forms subhedral crystals, which sometimes show rectilinear contacts with primary pyrite crystals now replaced by goethite (Figs. 9B, 9C and 9D). The magnetite crystals exhibit mild alteration to martite, which occurs irregularly or along crystallographic planes of magnetite. In the tonalite of subpopulation C_2, internal (int C Ilm; Fig. 9E) and external (ext C Ilm; Fig. 9F) composite ilmenite textures were observed (Buddington and Lindsley 1964, Haggerty 1991, Dall'Agnol *et al.* 1997).

Biotite monzogranite

All study samples of the BMzG group have relatively high MS (Tab. 3, Fig. 7E) and are distributed in populations B (subpopulation B_3) and C (subpopulations C_1 and C_2). The average modal content of opaque minerals of samples from subpopulation C_2 is higher than that of samples from subpopulations B_3 and C_1 (Tab. 2). In the BMzG samples, the most abundant opaque mineral is always magnetite followed by pyrite (± chalcopyrite) transformed into goethite. Only two samples from subpopulation C_2 contained ilmenite with hematite exsolutions and associated titanite (Tab. 3).

Magnetite is euhedral to subhedral and occurs included or associated with biotite lamellae, with which magnetite has

rectilinear contacts (Fig. 10A). In addition, magnetite crystals are commonly associated with pyrite crystals partly or fully replaced by goethite, and magnetite exhibits rectilinear or slightly irregular contacts with goethite (Figs. 10B and 10E). Magnetite was affected by the martitization process, whose intensity ranges from mild to moderate. Ilmenite crystals with titanite rims occur in only two samples from subpopulation C_2. Associated ilmenite and magnetite also occur in a sample from subpopulation C_2, and they show a titanite rim (Fig. 10F). The aspect of pyrite (Figs. 10C, 10D and 10E) is similar to that described in the BHTnl groups.

Hornblende-biotite granodiorite

The HBGd group also shows relatively high MS that mostly overlaps with the MS of BMzG (Tab. 3, Figs. 7E and 7F). As in the BMzG group, the average modal content of opaque minerals is clearly higher in subpopulation C_2 (Tabs. 2 and 3). With extremely rare exceptions, in this group, the most abundant opaque mineral is magnetite, which occurs as subhedral to euhedral crystals associated with or included in amphibole and biotite, which present rectilinear contacts with magnetite (Figs. 11A and 11B). Magnetite is slightly or moderately altered to martite. The pyrite-goethite association is the second-most abundant in this variety and both retain the textural characteristics
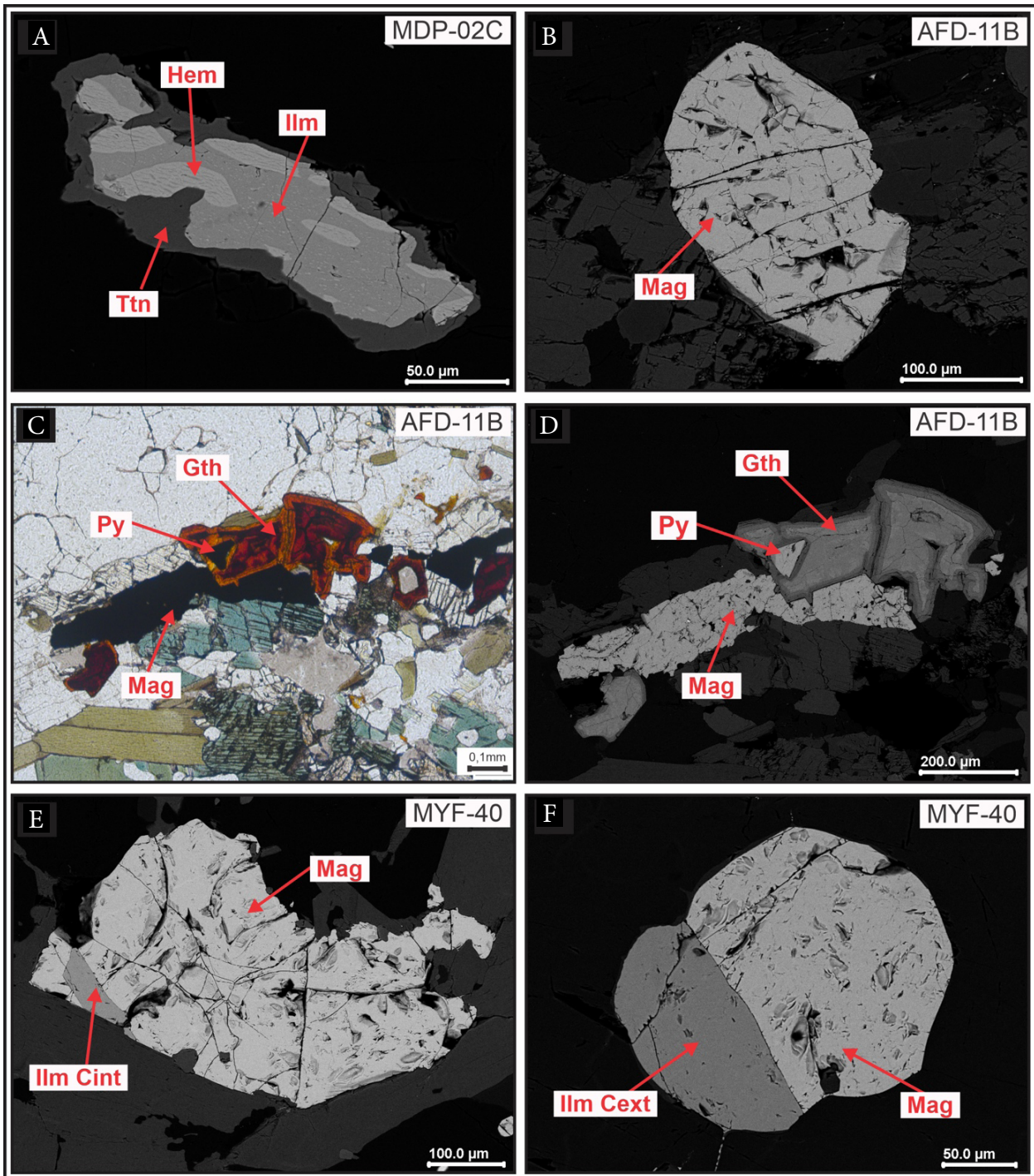
Figure 9. Textural aspects of dominant opaque minerals in representative samples of BHTnl: (A) ilmenite crystal surrounded by titanite rim, exhibiting hematite exsolution lamellae and hematite dominance zones with ilmenite lamellae; (B) subhedral magnetite crystal; (C and D) pyrite crystals almost entirely or entirely replaced by goethite and displaying rectilinear contact with subhedral magnetite crystals; (E and F) images of subhedral magnetite crystals locally with internal and external composite ilmenite, respectively. A, B, D, E, F: backscattered electron images acquired under SEM; C: flat polarized light photomicrograph of the same section observed in D. MDP-02C and AFD-11B = BHTnl from subpopulation B_2; MYF-40 = BHTnl from subpopulation C_2.

and its relationships with magnetite as described in the preceding subgroups (Figs. 11C and 11D). Ilmenite is present particularly in the samples of subpopulation B_3, although it is always scarce, and its crystals are surrounded by titanite rims and exhibit thin hematite exsolution lamellae (Figs. 11E and 11F).

Magnetite-rich syenogranites

In addition to the four varieties described above, the VJS contains PFR-14 (HBMzG) and MAR-119 (BHSnG) samples

that present very particular characteristics and differ significantly from the groups discussed earlier. Despite containing monzogranite, these samples will be described as magnetite-rich syenogranites (SnG) to distinguish them from the other groups. These samples have very high values of MS, belong to subpopulation C_2 (Tabs. 1 and 3, Fig. 7F), and sample MAR-119 shows the maximum MS value of the entire suite. The high MS values recorded in these two samples are consistent with their modal contents of opaque minerals and
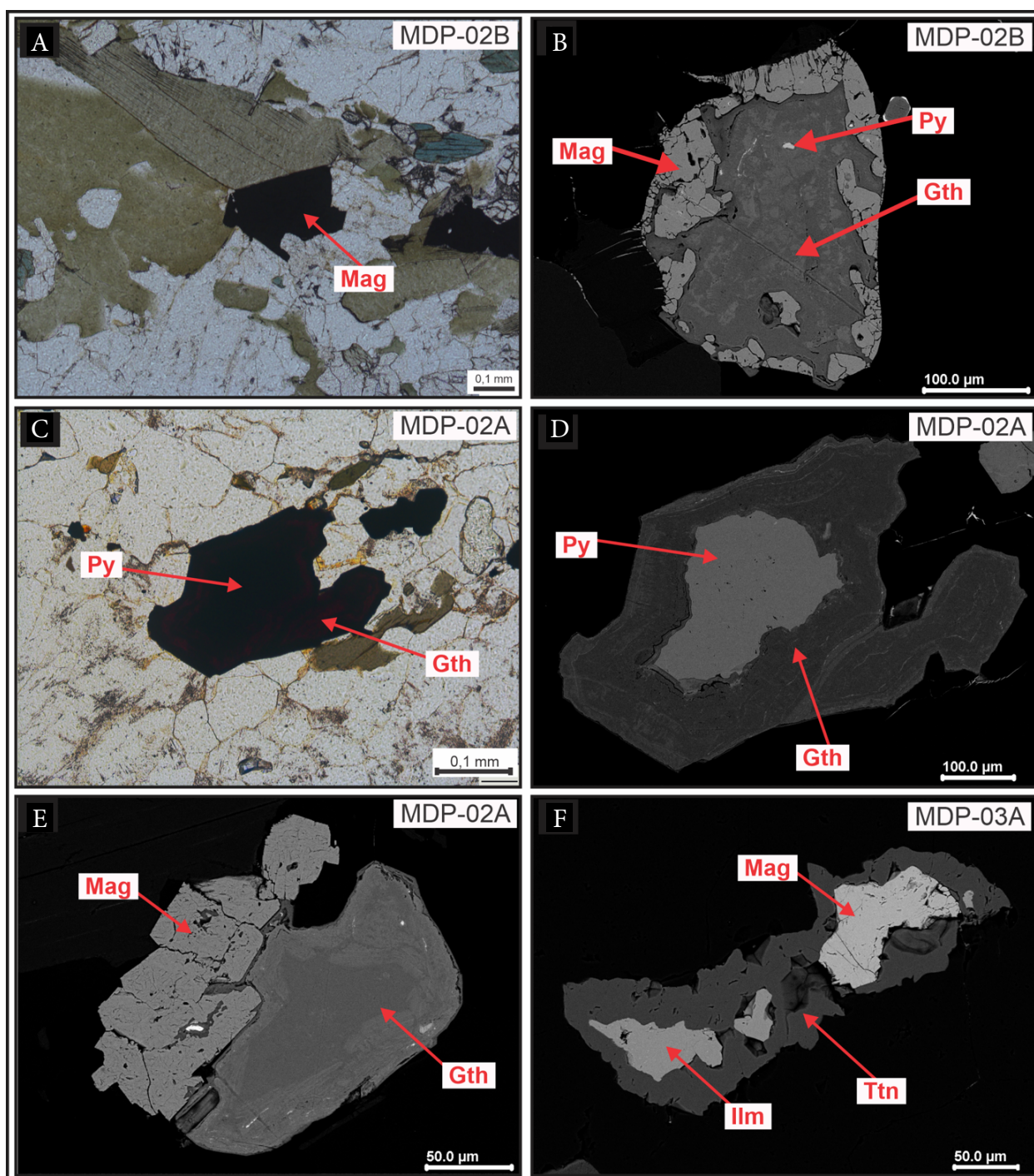
Figure 10. Textural aspects of dominant opaque minerals in samples representative of the BMzG group: (A) primary, subhedral magnetite crystal showing rectilinear contact with biotite; (B) pyrite crystal pseudomorphized in goethite, showing fine grains of magnetite on its boundaries (C) and (D) pyrite partly replaced by goethite; (E) primary magnetite crystals in regular contact with pyrite crystals fully replaced by goethite; (F) ilmenite crystal with very thin sparse hematite lamellae and magnetite crystal, both of which are surrounded by a titanite rim. A, C: Photomicrographs in flat polarized light showing the same section in C as in D; B, D, E, F: backscattered electron images acquired under SEM. MDP-02A = BMzG and MDP-02B = BGd from subpopulation B$_3$ and MDP-03A = BMzG from subpopulation C$_2$.

with the occurrence of slightly martitized magnetite as the only opaque mineral (Tab. 3, Suppl. Tab. A4). These rocks will be discussed separately from the other varieties.

Whole-rock FeO$_t$/(FeO$_t$ + MgO) ratios and mineral chemistry of amphibole and biotite

The new data on whole-rock chemical composition and new amphibole and biotite analyses performed in this study were integrated with the geochemical and mineral chemistry data published in previous studies (Dall'Agnol *et al.* 2017). Of the whole rock geochemistry data, only the FeO$_t$/(FeO$_t$ + MgO) ratios will be discussed in the present paper. These ratios and Fe/(Fe + Mg) data in amphibole and biotite are summarized in Tab. 3. Selected chemical compositions of amphibole and biotite are presented in Tabs. 4 and 5, respectively. In addition to the electron microprobe analysis, analyses of amphibole and biotite via EDS under an SEM were performed in this study (Suppl. Tabs. A1, A2, A3, and A4). EDS analyses are indicative only.
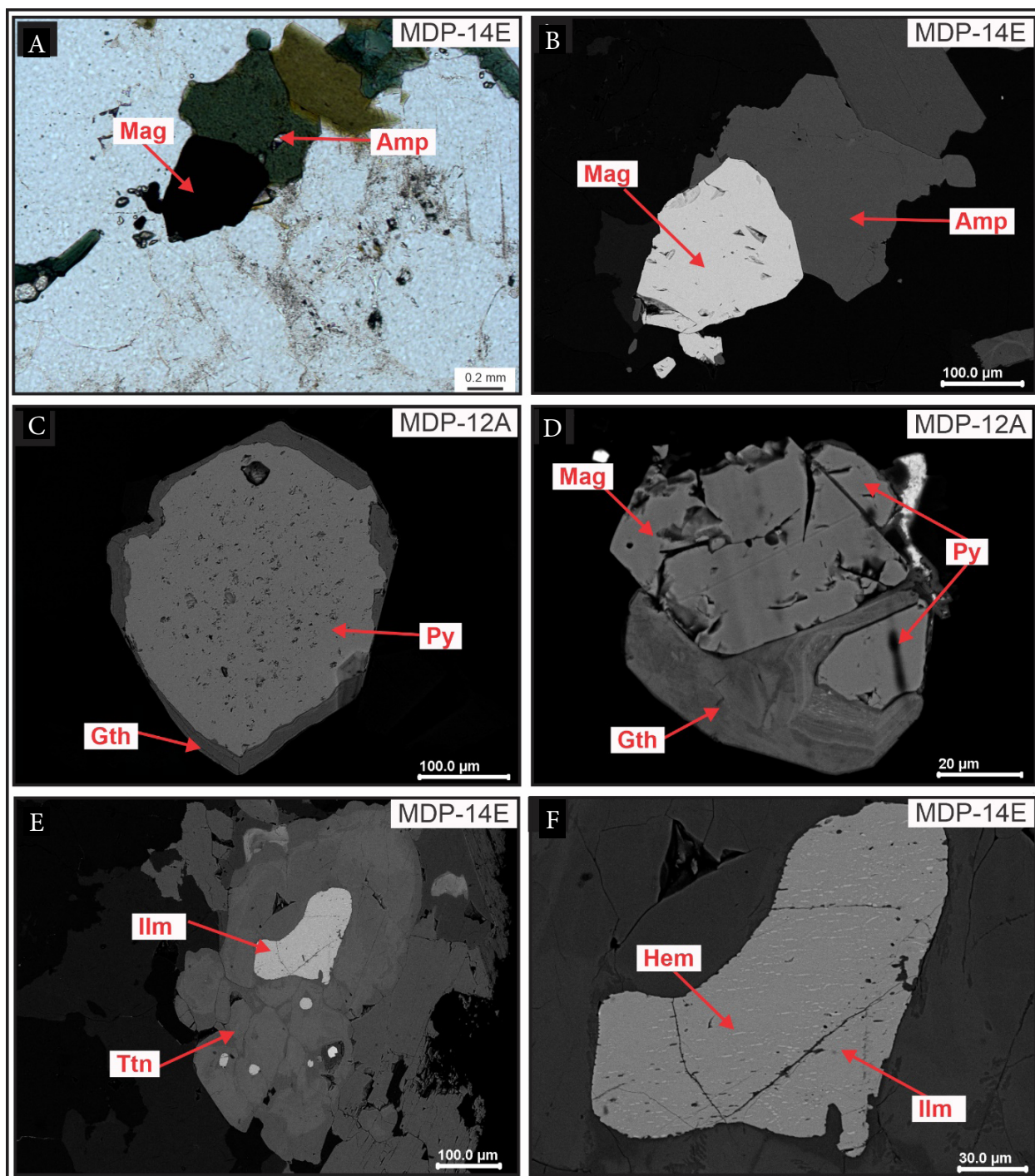
Figure 11. Textural aspects of dominant opaque minerals in samples representative of the HBGd group: (A and B) magnetite crystal exhibiting rectilinear contact with amphibole; (C) pyrite crystal with a fine goethite boundary; (D) magnetite crystal exhibiting rectilinear contact with pyrite partly replaced by goethite; (E and F) ilmenite crystal exhibiting hematite lamellae and surrounded by a titanite rim. A: flat polarized light photomicrograph; B, C, D, E, F: backscattered electron images acquired under SEM.

In terms of the whole-rock $FeO_t/(FeO_t+MgO)$ ratio (Tab. 3), samples from subgroup 1 (population A and subpopulation B_1) of the biotite-hornblende monzogranite (BHMzG) group tend to show values ≥ 0.90, whereas those of subgroup 2 (subpopulations B_3 and C_1) ranged from 0.84 to 0.89. The Fe/(Fe + Mg) ratios in amphibole and biotite also decrease markedly from the samples of population A of subgroup 1 to those of subpopulation B_1 of the same group, attaining the lowest values in the samples of subgroup 2 (Tab. 3).

The rocks from the biotite-hornblende tonalite (BHTnl) group display $FeO_t/(FeO_t + Mg)$ ratios ranging from 0.75 to 0.76 with an anomalous value of 0.85 (Tab. 3). Amphibole and biotite showed moderate Fe/(Fe + Mg) ratios and display significant variations in the samples of subpopulations B_2 and C_2 (Tabs. 3, 4, and 5).

The whole-rock $FeO_t/(FeO_t+MgO)$ ratios found in samples from biotite monzogranite (BMzG) ranged from 0.78 to 0.81 and show little variation in the different subpopulations (Tab. 3). The Fe/(Fe + Mg) ratios in amphibole and biotite display moderate values and are similar in the different analyzed subpopulations (Tabs. 3, 4, and 5).

The whole-rock $FeOt/(FeOt + MgO)$ ratios of samples from the hornblende-biotite granodiorite (HBGd) group

is directly associated with the behavior of magnetite, which is the main ferromagnetic mineral (Clark 1999).

In the BHMzG, the low MS values of subgroup 1 can be explained by the dominance of ilmenite and the differences in MS between samples from populations A and B_1 are due to the presence of a small fraction of magnetite in the samples of subpopulation B_1 (Tabs. 1 and 3). The significant occurrence and dominance of magnetite in subgroup 2 justifies its magnetic signature with relatively higher MS values than those in subgroup 1.

The samples of subpopulation B_2 of the BHTnl display moderate values of MS that reflect the dominance of sulfides over magnetite. The sample of subpopulation C_2 has magnetite as the main opaque phase and shows higher MS compared to the rocks of subpopulation B_2 (Tab. 3).

The samples of the BMzG group display moderate to high MS (Tab. 3, Fig. 7E) and are distributed in populations B (subpopulation B_3) and C (subpopulations C_1 and C_2). In the BMzG and HBGd, magnetite is the most abundant opaque mineral followed by pyrite transformed into goethite. Only two samples from subpopulation C_2 of the BMzG contained ilmenite with hematite exsolutions and associated titanite. In the HBGd, ilmenite is rare or even absent (Tab. 3).

Table 4. Selected electron microprobe analyses and structural formulae for amphibole of the granitoids of the Vila Jussara Suite.

Petrographic varieties	Biotite-hornblende monzogranite (BHMzG)						Biotite-hornblende tonalite (BHTnl)						Biotite-hornblende Syenogranite (HSnG)	
Magnetic population	Population A		Subpopulation B1		Subpopulation C1		Subpopulation B2				Subpopulation C2		Subpopulation C2	
Sample	PFR-16A*		MDP-57A**		PFA-39**		PFA-62*		MDP-02C**		MYF-40*		MAR-119*	
Analysis	C1	C1	C1	C2	C1	C2	C3	C3	C1	C3	C1	C3	C3	C4
	Amph	Amph	Amph	Amph	Amph	Amph	Amph	Amph	Amph	Amph	Amph	Amph	Amph	Amph
	1-2	4-4	1-4	1-1	1-2	1-5	1-6	2-6	1-2	1-1	2-5	2-2	2-6	1-2
SiO_2 (Wt%)	37.37	37.34	37.48	37.30	37.74	38.89	39.39	40.20	40.64	38.99	41.89	42.27	36.27	36.21
TiO_2	0.47	0.59	0.77	0.67	0.70	0.79	1.23	1.58	1.43	0.60	1.45	1.59	0.49	0.58
Al_2O_3	12.52	12.66	12.21	12.30	12.24	11.58	11.30	10.40	10.59	12.17	10.32	10.11	12.66	12.62
Fe_2O_3	5.70	4.79	8.42	8.71	7.33	6.35	5.59	5.12	5.71	8.13	5.18	5.23	7.42	8.07
FeO	24.70	25.32	20.79	20.86	20.57	20.68	20.03	20.71	16.35	15.78	15.46	15.81	24.15	23.77
MnO	0.59	0.55	0.48	0.45	0.57	0.61	0.42	0.43	0.42	0.49	0.54	0.53	0.86	0.79
MgO	1.48	1.39	2.59	2.40	3.80	4.24	5.05	5.34	7.45	6.42	8.54	8.53	0.84	0.93
CaO	10.80	10.94	9.88	9.97	10.70	10.89	10.83	10.94	10.88	10.80	11.18	11.22	10.39	10.38
Na_2O	1.31	1.24	1.57	1.43	1.56	1.52	1.59	1.73	1.65	1.49	1.59	1.62	1.38	1.31
K_2O	2.43	2.49	2.10	2.09	2.39	1.98	1.92	1.75	1.53	1.91	1.52	1.48	2.61	2.61
F	0.15	0.24	0.13	0.18	0.00	0.01	0.00	0.00	0.15	0.23	0.29	0.32	0.10	0.08
Cl	1.21	1.27	1.48	1.54	0.02	0.09	1.34	1.25	0.53	0.71	0.21	0.21	1.94	1.93
H_2O*	1.47	1.41	1.42	1.38	1.87	1.86	1.56	1.60	1.72	1.63	1.77	1.77	1.29	1.30
Subtotal	100.21	100.21	99.31	99.28	99.48	99.49	100.25	101.05	99.05	99.35	99.93	100.68	100.39	100.58
O=F,Cl	0.34	0.39	0.39	0.42	0.01	0.03	0.30	0.28	0.18	0.26	0.17	0.18	0.48	0.47
Total	99.88	99.82	98.93	98.86	99.48	99.46	99.95	100.77	98.86	99.09	99.76	100.50	99.91	100.11
Number of cations per formulae unit based on twenty three oxygen atoms														
Si	6.06	6.07	6.06	6.04	6.02	6.16	6.21	6.29	6.32	6.10	6.39	6.41	5.94	5.92
Al^{iv}	1.94	1.93	1.94	1.96	1.98	1.84	1.79	1.71	1.68	1.90	1.61	1.59	2.06	2.08
Al^{vi}	0.46	0.49	0.38	0.39	0.32	0.33	0.31	0.20	0.26	0.35	0.25	0.22	0.39	0.35
Ti	0.06	0.07	0.09	0.08	0.08	0.09	0.15	0.19	0.17	0.07	0.17	0.18	0.06	0.07
Fe^{3+}	0.70	0.59	1.02	1.06	0.88	0.76	0.66	0.60	0.67	0.96	0.59	0.60	0.92	0.99
Fe^{2+}	3.35	3.44	2.81	2.83	2.74	2.74	2.64	2.71	2.13	2.07	1.97	2.01	3.31	3.25
Mn	0.08	0.08	0.07	0.06	0.08	0.08	0.06	0.06	0.06	0.07	0.07	0.07	0.12	0.11
Mg	0.36	0.34	0.62	0.58	0.90	1.00	1.19	1.24	1.73	1.50	1.94	1.93	0.20	0.23
Ca	1.88	1.90	1.71	1.73	1.83	1.85	1.83	1.83	1.81	1.81	1.83	1.82	1.82	1.82
Na	0.41	0.39	0.49	0.45	0.48	0.47	0.48	0.52	0.50	0.45	0.47	0.48	0.44	0.41
K	0.50	0.52	0.43	0.43	0.49	0.40	0.39	0.35	0.30	0.38	0.30	0.29	0.54	0.54
Fe/(Fe+Mg)	0.903	0.911	0.818	0.830	0.752	0.733	0.690	0.685	0.552	0.580	0.504	0.510	0.942	0.935

Table 4. Continuation.

Petrographic varieties	Hornblende-biotite granodiorite (HBGd)								Biotite monzogranite (BMzG)			
Magnetic population	Subpopulation B3		Subpopulation C1				Subpopulation C2		Subpopulation C1		Subpopulation C2	
Sample	AFD-11A**		ADE-01D**		AFD-16A**		AFD-08*		MDP-55**		LIF-04A**	
	C1	C1	C1	C2	C2	C2	C1	C1	C4	C3	C2	C3
Analysis	Amph 1-1	Amph 1-5	Amph 1-3	Amph 1-3	Amph-1-3	Amph 2-4	Amph 2-1	Amph 2-8	Amph 1-3	Amph 1-1	Amph 1-1	Amph 1-3
SiO_2 (Wt%)	37,80	38.31	38.81	39.07	38.95	38.49	39.91	39.52	38.42	38.29	38.17	38.42
TiO_2	0.44	0.59	0.54	0.56	0.58	0.62	0.72	0.69	0.51	0.49	0.42	0.40
Al_2O_3	12.59	12.41	12.47	12.54	11.90	12.33	11.58	12.10	12.66	12.69	12.79	12.76
Fe_2O_3	7.00	6.47	6.09	6.97	7.66	7.43	6.54	6.10	7.53	7.59	7.70	7.99
FeO	19.84	19.85	19.62	19.47	17.48	18.19	18.14	18.45	17.12	17.54	16.55	16.33
MnO	0.44	0.46	0.44	0.43	0.57	0.57	0.56	0.56	0.59	0.56	0.67	0.70
MgO	4.17	4.39	4.91	4.70	5.67	5.20	6.01	5.83	5.55	5.25	5.66	5.76
CaO	10.77	10.81	10.92	10.85	10.79	10.89	11.11	11.17	10.74	10.65	10.79	10.80
Na_2O	1.45	1.44	1.62	1.55	1.50	1.43	1.53	1.53	1.55	1.61	1.52	1.51
K_2O	2.35	2.25	2.20	2.12	2.10	2.20	1.90	2.07	2.11	2.10	2.00	1.96
F	0.13	0.00	0.04	0.00	0.15	0.06	0.19	0.20	0.44	0.41	0.23	0.35
Cl	0.02	0.09	0.00	0.06	0.86	0.94	0.68	0.80	0.69	0.67	0.59	0.61
H_2O*	1.81	1.86	1.89	1.90	1.62	1.63	1.67	1.63	1.52	1.53	1.63	1.59
Subtotal	98.82	98.92	99.55	100.22	99.83	99.97	100.53	100.64	99.44	99.38	98.72	99.15
O=F,Cl	0.06	0.02	0.02	0.01	0.26	0.24	0.23	0.27	0.34	0.32	0.23	0.28
Total	98.76	98.90	99.53	100.21	99.57	99.73	100.29	100.38	99.10	99.06	98.49	98.87
Number of cations per formulae unit based on twenty three oxygen atoms												
Si	6.03	6.09	6.11	6.11	6.12	6.06	6.20	6.15	6.05	6.05	6.04	6.05
Al^{iv}	1.97	1.91	1.89	1.89	1.88	1.94	1.80	1.85	1.95	1.95	1.96	1.95
Al^{vi}	0.40	0.41	0.42	0.42	0.33	0.35	0.33	0.37	0.41	0.41	0.42	0.41
Ti	0.05	0.07	0.06	0.07	0.07	0.07	0.08	0.08	0.06	0.06	0.05	0.05
Fe^{3+}	0.84	0.77	0.72	0.82	0.91	0.88	0.76	0.72	0.89	0.90	0.92	0.95
Fe^{2+}	2.65	2.64	2.58	2.55	2.30	2.40	2.36	2.40	2.26	2.32	2.19	2.15
Mn	0.06	0.06	0.06	0.06	0.08	0.08	0.07	0.07	0.08	0.07	0.09	0.09
Mg	0.99	1.04	1.15	1.09	1.33	1.22	1.39	1.35	1.30	1.24	1.33	1.35
Ca	1.84	1.84	1.84	1.82	1.82	1.84	1.85	1.86	1.81	1.80	1.83	1.82
Na	0.45	0.44	0.49	0.47	0.46	0.44	0.46	0.46	0.47	0.49	0.46	0.46
K	0.48	0.46	0.44	0.42	0.42	0.44	0.38	0.41	0.42	0.42	0.40	0.39
Fe/(Fe+Mg)	0.727	0.717	0.691	0.699	0.634	0.663	0.629	0.640	0.634	0.652	0.621	0.614

Lower limit of detection (LLD in ppm): Si = 51; Ti = 98; Al = 26; Fe = 92; Mn = 70; Mg = 38; Ca = 55; Na = 28; K = 30; F = 165; Cl = 14. Data source: *Dall'Agnol et al. 2017; **this work.

range from 0.76 to 0.83 and do not vary significantly in the different subpopulations (Tab. 3). The mineral chemistry data collected in electron microprobe analyses in amphiboles have similar Fe/(Fe + Mg) ratios in samples of subpopulations C_1 and C_2, whereas the same ratio shows significant variations in biotite and decreases from subpopulation C_1 to C_2 (Tabs. 3, 4 and 5).

The MAR-119 sample of the BHSnG group has the highest whole-rock $FeO_t/(FeO_t + MgO)$ ratio of the entire study set (0.99; Tab. 3), and the PFR-14 sample shows similar behavior. The electron microprobe analysis of amphibole in sample MAR-119 revealed Fe/Fe + Mg ratios ranging from 0.93 to 0.95, which is compatible with the extreme values obtained for the whole-rock $FeO_t/(FeO_t + MgO)$ ratio (Tab. 3).

DISCUSSION

Iron-titanium oxide minerals and magnetic susceptibility

The MS of rocks essentially depends on the modal content, nature, and occurrence mode of its ferromagnetic minerals. In granitoids composed of quartz, feldspars, ferromagnesian silicates, and accessory minerals, the variation in MS

Finally, the BHSnG shows very high values of MS and belongs to subpopulation C$_2$ (Tabs. 1 and 3, Fig. 7F). This is a consequence of the total dominance and high modal contents of magnetite in these rocks.

In some samples of different varieties, magnetite was partially replaced for martite and this alteration contributed to a reduction in MS values. However, this alteration process was not intense and certainly should not significantly affect the MS values of the rocks studied.

The MS data associated with the behavior of Fe-Ti oxide minerals provided a logical overview of the variations in MS observed in the different granite varieties and helped gain a better understanding of the complex magnetic behavior of the VJS. The presence of BHMzG of subgroup 2 in the subpopulation B$_3$, together with the BMzG and HBGd samples, can be explained by the relatively high modal content of magnetite in all these rocks. In the same way, the presence of the BHSnG in the subpopulation C$_2$, side by side with the BMzG and HBGd samples, is due to the extremely high magnetite modal content of the former.

Classification of the Vila Jussara granitoids based on whole rock FeOt/ (FeOt + MgO)

The geochemical behavior of the Vila Jussara granitoids was discussed in detail by Dall'Agnol *et al.* (2017). In this study, we only intend to put in evidence some peculiar characteristics of the granitoids studied. For that, the whole rock FeOt/

Table 5. Selected electron microprobe analyses and structural formulae for biotite of the granitoids of the Vila Jussara Suite.

Petrographic varieties	Biotite-hornblende monzogranite (BHMzG)						Biotite-hornblende tonalite (BHTnl)					
Magnetic population	Population A	Subpopulation B1		Subpopulation C1			Subpopulation B2				Subpopulation C2	
Sample	PFR-16A*	MDP-57A**		PFA-39**			PFA-62*		MDP-02C**		MYF-40*	
	C1	C1	C2	C3	C1	C2	C1	C2	C2	C3	C2	C4
Analysis	Biot 1-5	Biot 1-10	Biot 1-1	Biot 1-4	Biot 1-2	Biot 1-2	Biot 1-5	Biot 3-3	Biot 1-4	Biot 1-5	Biot 2-1	Biot 1-1
SiO$_2$ (wt %)	34.47	34.64	34.07	34.13	35.43	35.51	35.14	34.94	36.16	36.15	36.69	36.13
TiO$_2$	2.21	2.22	3.09	2.86	2.74	2.46	4.15	4.25	2.17	2.27	3.81	3.77
Al$_2$O$_3$	14.33	14.61	14.44	14.69	14.61	14.62	13.65	13.56	14.67	14.66	14.03	13.89
FeO	30.78	31.24	29.40	28.83	25.54	25.43	26.55	26.72	21.32	21.27	21.81	20.99
MnO	0.42	0.37	0.34	0.36	0.34	0.36	0.22	0.14	0.28	0.29	0.32	0.29
MgO	2.74	2.85	4.19	4.60	7.28	7.44	6.75	7.01	10.31	10.22	10.18	10.46
CaO	0.05	0.03	0.01	0.02	0.02	0.03	0.03	0.16	0.04	0.01	0.03	0.00
Na$_2$O	0.09	0.09	0.05	0.09	0.07	0.06	0.07	0.07	0.07	0.06	0.06	0.06
K$_2$O	9.03	9.15	8.80	8.86	9.32	9.29	9.21	8.88	9.12	9.23	9.66	9.62
F	0.00	0.03	0.23	0.18	0.32	0.47	0.00	0.04	0.56	0.67	0.52	0.52
Cl	0.81	0.81	0.95	0.89	0.85	0.82	0.84	0.75	0.39	0.38	0.19	0.19
H$_2$O	3.44	3.46	3.34	3.39	3.44	3.37	3.59	3.59	3.48	3.43	3.63	3.58
Subtotal	98.77	99.83	99.55	99.57	100.49	100.56	101.09	101.07	98.96	98.90	101.26	99.91
O=F,Cl	0.18	0.20	0.31	0.28	0.33	0.38	0.19	0.18	0.32	0.37	0.26	0.26
Total	98.59	99.63	99.24	99.29	100.16	100.17	100.90	100.89	98.63	98.53	101.00	99.65
Number of cations per formulae unit based on twenty two oxygen atoms												
Si	5.665	5.635	5.536	5.527	5.584	5.596	5.543	5.512	5.640	5.641	5.606	5.587
Al ^{iv}	2.335	2.365	2.464	2.473	2.416	2.404	2.457	2.488	2.360	2.359	2.394	2.413
Al ^{vi}	0.440	0.437	0.302	0.330	0.297	0.313	0.082	0.033	0.337	0.338	0.132	0.118
Ti	0.273	0.271	0.378	0.349	0.325	0.291	0.492	0.504	0.254	0.267	0.438	0.439
Fe	4.231	4.251	3.995	3.905	3.366	3.352	3.503	3.525	2.781	2.776	2.787	2.715
Mn	0.059	0.051	0.047	0.050	0.046	0.048	0.029	0.019	0.036	0.038	0.041	0.039
Mg	0.672	0.690	1.016	1.109	1.710	1.748	1.587	1.648	2.397	2.377	2.319	2.412
Ca	0.009	0.005	0.002	0.003	0.004	0.004	0.005	0.027	0.007	0.002	0.005	0.000
Na	0.030	0.028	0.017	0.028	0.021	0.019	0.023	0.022	0.022	0.019	0.016	0.019
K	1.894	1.899	1.825	1.830	1.873	1.867	1.853	1.786	1.815	1.837	1.883	1.896
Al total	2.775	2.802	2.766	2.803	2.713	2.716	2.538	2.522	2.696	2.696	2.526	2.531
Fe/Fe+Mg	0.863	0.860	0.797	0.779	0.663	0.657	0.688	0.681	0.537	0.539	0.546	0.530

Table 5. Continuation.

Petrographic varieties	Biotite monzogranite (BMzG)				Hornblende-biotite granodiorite (HBGd)							
Magnetic population	Subpopulation C1				Subpopulation B3		Subpopulation C1				Subpopulation C2	
Sample	MDP-55**		LIF-04A**		AFD-11A**		ADE-01D**		AFD-16A**		AFD-08*	
	C4	C3	C1	C3	C1	C1	C1	C1	C1	C3	C1	C2
Analysis	Biot 1-3	Biot 1-4	Biot 1-4	Biot 1-2	Biot 1-1	Biot 1-5	Biot 1-1	Biot 1-3	Biot 1-12	Biot 2-2	Biot 1-1	Biot 1-4
SiO_2 (wt %)	36.15	36.59	36.03	36.21	35.92	36.02	36.42	36.22	36.19	36.32	36.38	36.31
TiO_2	2.27	2.06	1.79	1.96	1.93	2.14	1.65	1.58	1.63	2.10	1.90	2.07
Al_2O_3	14.74	14.91	14.64	14.88	14.83	14.65	14.70	14.62	14.74	14.65	14.76	14.64
FeO	21.80	21.68	21.48	21.53	25.19	24.94	23.04	23.10	23.49	23.13	22.63	22.77
MnO	0.38	0.38	0.46	0.54	0.31	0.33	0.31	0.32	0.43	0.43	0.36	0.36
MgO	9.65	9.78	10.34	10.22	7.70	7.86	9.16	9.12	8.91	8.95	9.54	9.49
CaO	0.01	0.00	0.02	0.03	0.02	0.01	0.10	0.08	0.01	0.02	0.06	0.05
Na_2O	0.04	0.04	0.06	0.06	0.10	0.07	0.07	0.08	0.02	0.06	0.11	0.05
K_2O	9.13	9.17	9.11	9.21	9.36	9.42	9.48	9.43	9.58	9.43	9.67	9.47
F	1.12	1.07	0.73	0.83	0.48	0.50	0.61	0.62	0.45	0.55	0.53	0.56
Cl	0.32	0.32	0.38	0.36	0.61	0.59	0.39	0.39	0.52	0.44	0.44	0.42
H_2O	3.22	3.28	3.38	3.37	3.43	3.44	3.45	3.42	3.48	3.47	3.50	3.48
Subtotal	99.02	99.57	98.64	99.55	99.98	100.21	99.58	99.03	99.65	99.94	99.97	99.91
O=F,Cl	0.54	0.52	0.39	0.43	0.34	0.34	0.34	0.35	0.31	0.33	0.32	0.33
Total	98.47	99.05	98.25	99.11	99.64	99.87	99.23	98.68	99.34	99.61	99.65	99.58
Number of cations per formulae unit based on twenty two oxygen atoms												
Si	5.653	5.680	5.645	5.629	5.649	5.652	5.691	5.690	5.671	5.666	5.654	5.651
Al^{iv}	2.347	2.320	2.355	2.371	2.351	2.348	2.309	2.310	2.329	2.334	2.346	2.349
Al^{vi}	0.370	0.409	0.349	0.355	0.397	0.362	0.398	0.397	0.393	0.360	0.358	0.338
Ti	0.267	0.240	0.211	0.229	0.228	0.252	0.194	0.186	0.192	0.246	0.222	0.242
Fe	2.851	2.815	2.815	2.800	3.313	3.273	3.011	3.035	3.079	3.018	2.941	2.964
Mn	0.050	0.050	0.060	0.071	0.041	0.043	0.041	0.042	0.057	0.057	0.048	0.047
Mg	2.249	2.263	2.416	2.368	1.804	1.838	2.133	2.136	2.081	2.080	2.211	2.202
Ca	0.002	0.001	0.004	0.005	0.004	0.001	0.017	0.013	0.002	0.003	0.010	0.008
Na	0.012	0.013	0.019	0.017	0.032	0.023	0.020	0.023	0.007	0.019	0.034	0.015
K	1.820	1.816	1.821	1.826	1.877	1.885	1.889	1.889	1.914	1.877	1.917	1.881
Al total	2.717	2.729	2.704	2.727	2.748	2.710	2.707	2.708	2.722	2.694	2.704	2.686
Fe/Fe+Mg	0.559	0.554	0.538	0.542	0.647	0.640	0.585	0.587	0.597	0.592	0.571	0.574

Total Fe reported as FeO. Lower limit of detection (LLD in ppm): Si = 51; Ti = 98; Al = 26; Fe = 92; Mn = 70; Mg = 38; Ca = 55; Na = 28; K = 30; F = 165; Cl = 14. Data source: *Dall'Agnol et al. 2017; **this work.

(FeOt + MgO) ratio of selected analyzed samples of the VJS (data from Dall'Agnol *et al.* 2017, Silva *et al.* 2020, this work) were plotted in the FeO/(FeO + MgO) vs. SiO_2 (Frost *et al.* 2001) and FeO/(FeO + MgO) vs. Al_2O_3 diagrams (Figs. 12A and 12B). In both diagrams, there is a net distinction between the BHMzG and BHSnG varieties and the BHTnl, BMzG, and HBGd ones, with the latter plotting in the magnesian or calc-al-kaline (Cordilleran) field and the former in the ferroan granite field. Besides, it is possible to verify the contrast between the BHMzG of population A and subpopulation B_1 which have characteristics of reduced A-type granites, whereas those of subgroup 2 are classified as oxidized A-type granites (Fig. 12B).

These diagrams reveal the particular geochemical behavior of the VJS, which shows a trace-element geochemical signature akin to A-type granites but is formed by granitoids varying from ferroan to magnesian granites (Fig. 12A; *cf.* Dall'Agnol *et al.* 2017). Another relevant point is that, according to the selected diagrams, the BHSnG can be unequivocally classified as a reduced A-type (ferroan) granite (Fig. 12B), even if containing a relatively high modal content of magnetite and high MS value. The peculiar geochemical behavior of the Vila Jussara granitoids is strictly associated with strong variations in oxygen fugacity and magnetic petrology that are not commonly observed in granitoid suites.

Oxygen fugacity estimate for granitoids of the Vila Jussara Suite

There are no objective conditions to apply the oxybarom-eter based on primary compositions of Fe-Ti oxide minerals

(Buddington and Lindsley 1964, Dall'Agnol *et al.* 1997) because these minerals were reequilibrated. However, the associations between Fe-Ti oxide minerals and iron-bearing silicate phases as well as the Fe/(Fe + Mg) ratios of the latter and the [FeOt/(FeOt + MgO)] of whole-rock provide information for estimating the prevailing fO_2 conditions during magmatic crystallization. These data are summarized in Tab. 3 and shown in more detail in Suppl. Tabs. A1, A2, A3, and A4.

In granite systems, the prevailing fO_2 in the magma source and during differentiation processes has implications for magmatic evolution and crystallization (Wones 1981, Ishihara 1981, Frost 1991, Haggerty 1991, Dall'Agnol *et al.* 1997). Several theoretical and experimental studies were conducted to estimate fO_2 and understand its role both in the origin of magmas and throughout their differentiation (Buddington and Lindsley 1964, Wones and Eugster 1965, Carmichael 1991, Frost 1991, Frost and Lindsley 1992, Anderson and Smith 1995, Anderson *et al.* 2008, Ghiorso and Evans 2008, Ridolfi *et al.* 2010, Putirka 2016, Arató and Audétat 2017; *cf.* also Loucks *et al.* 2018, for a critical review of fO_2 evolution in magmatic rocks).

The available set of petrographic, ineralogyical, and geochemical data on the granitoids of the VJS was employed to empirically estimate the oxygen fugacity conditions of the formation of each group of rocks. The Fe/(Fe + Mg) ratios in amphibole and biotite of the granites studied (Figs. 12C and 12D) indicate the oxygen fugacity prevalent during their crystallization (*cf.* Czamanske and Mihalik 1972, Ishihara 1981, Anderson and Smith 1995, Anderson *et al.* 2008, Cunha *et al.* 2016, Dall'Agnol *et al.* 2017). These data were associated with the nature of Fe-Ti oxide minerals and the [FeOt/(FeOt + MgO)] of whole rock to estimate the prevalent oxygen fugacity during the crystallization of each granite variety (Fig. 12E). The absence of magnetite indicates formation at fO_2 conditions below the FMQ buffer and its occurrence indicates comparatively higher fO_2, on or above FMQ, that could attain NNO buffer conditions.

In Fig. 12E, temperature intervals of crystallization for each variety were based on estimates by Dall'Agnol *et al.* (2017) and additional unpublished data obtained by the authors, in both cases using amphibole composition and applying the method of Ridolfi *et al.* (2010). We assumed that fO_2 conditions evolved with decreasing temperature in parallel with the buffer curves. This is commonly the case, but Loucks *et al.* (2018) consider that several magmatic suites changed their fO_2 trends relative to reference buffers during magmatic evolution. They concluded that in suites with low-water contents, there was a tendency of fO_2 decrease during magmatic evolution, the opposite being observed in water-rich suites. Besides, fugacity estimates based only on the composition of mafic minerals (Anderson and Smith 1995) are, to some degree, an oversimplification. However, when they are associated with modal iron-titanium oxide minerals and the [FeOt/(FeOt + MgO)] of whole-rock, better estimates of fO_2 conditions are possible.

The BHMzG of population A from subgroup 1 were formed outside the magnetite stability field, their whole-rock FeOt/(FeOt + MgO) ratios are compatible with reduced type A granites (Figs. 12A and 12B), their amphibole compositions indicate formation under low fO_2, and their biotite corresponds to the mica of the ilmenite series (Figs. 12C and 12D; Suppl. Tab. A1). Based on these data, they likely evolved under reduced conditions (Fig. 12E), and the trajectory was slightly below the fayalite-magnetite-quartz buffer curve (FMQ; buffer curves according to Frost 1991). On the other hand, the BHMzG of subpopulation B_1 from subgroup 1 has also ilmenite but it already contains primary magnetite and the whole-rock FeOt/(FeOt + MgO) ratios are equivalent to those of reduced or oxidized A-type granites (Fig. 12B), amphibole compositions indicate low or transitional (low to intermediate) fO_2 conditions, and the biotite have compositions comparable to those of mica minerals of the ilmenite series or of biotite from transitional granites between the ilmenite and magnetite series (Figs. 12C and 12D; Suppl. Tab. A1). This dataset suggests the formation of this variety under moderately reduced conditions, over the FMQ buffer curve, or only slightly above it (Fig. 12E). In the BHMzG of subgroup 2, magnetite dominates over ilmenite (Tab. 3, Suppl. Tab. A1). Their whole-rock FeOt/(FeOt + MgO) ratios are similar to those of oxidized type A granites (Fig. 12B); their amphibole composition indicates formation under low fO_2 (Suppl. Tab. A1) to intermediate fO_2 (Fig. 12C); and their biotite composition is mostly transitional between the biotite of granites of the ilmenite and magnetite series (Suppl. Tab. A1). Such granites formed certainly above the FMQ buffer, but most likely below the NNO buffer, and their fO_2 conditions were estimated as being equivalent to FMQ+0.5 (Fig. 12E).

The dominant samples from the BHTnl group are characterized by pyrite dominance followed by magnetite, with the inverse occurring only in sample MYF-40 (Tab. 3, Suppl. Tab. A2). Their whole-rock FeOt/(FeOt+MgO) ratios indicate that they are magnesian granites, except for sample PFA-62 (Figs. 12a and 12b; Tab. A2). Amphibole compositional data (Fig. 12C; Suppl. Tab. A2) indicate formation under intermediate or high fO_2 conditions and biotite has always displayed similarity with the biotite of granites of the magnetite series (Fig. 12D; Suppl. Tab. A2). In conclusion, this granitoid crystallized under oxidizing conditions is equivalent to NNO to NNO-0.5 or in the case of sample MYF-40 to NNO+1 (Fig. 12E).

In the BMzG, the dominant opaque phase is magnetite (Tab. 3, Suppl. Tab. A3). Their whole-rock FeOt/(FeOt + MgO) ratios make it possible to classify them as magnesian granites (Fig. 12A), their amphibole composition indicates crystallization under intermediate or transitional between intermediate to high fO_2 conditions (Fig. 12C), and their biotite composition is equivalent to the mica composition of granitoids of the magnetite series (Fig. 12D; Suppl. Tab. A3). Such granitoids crystallized under oxidizing conditions likely corresponding to NNO to NNO+0.5 based on empirical data (Fig. 12E). In turn, rocks from the HBGd group show strong analogies with the BMzG in terms of dominant opaque minerals (Tab. 3, Suppl. Tabs. A3 and A4) and whole-rock FeOt/(FeOt + MgO) ratios (Figs. 12A and 12B). The results clearly
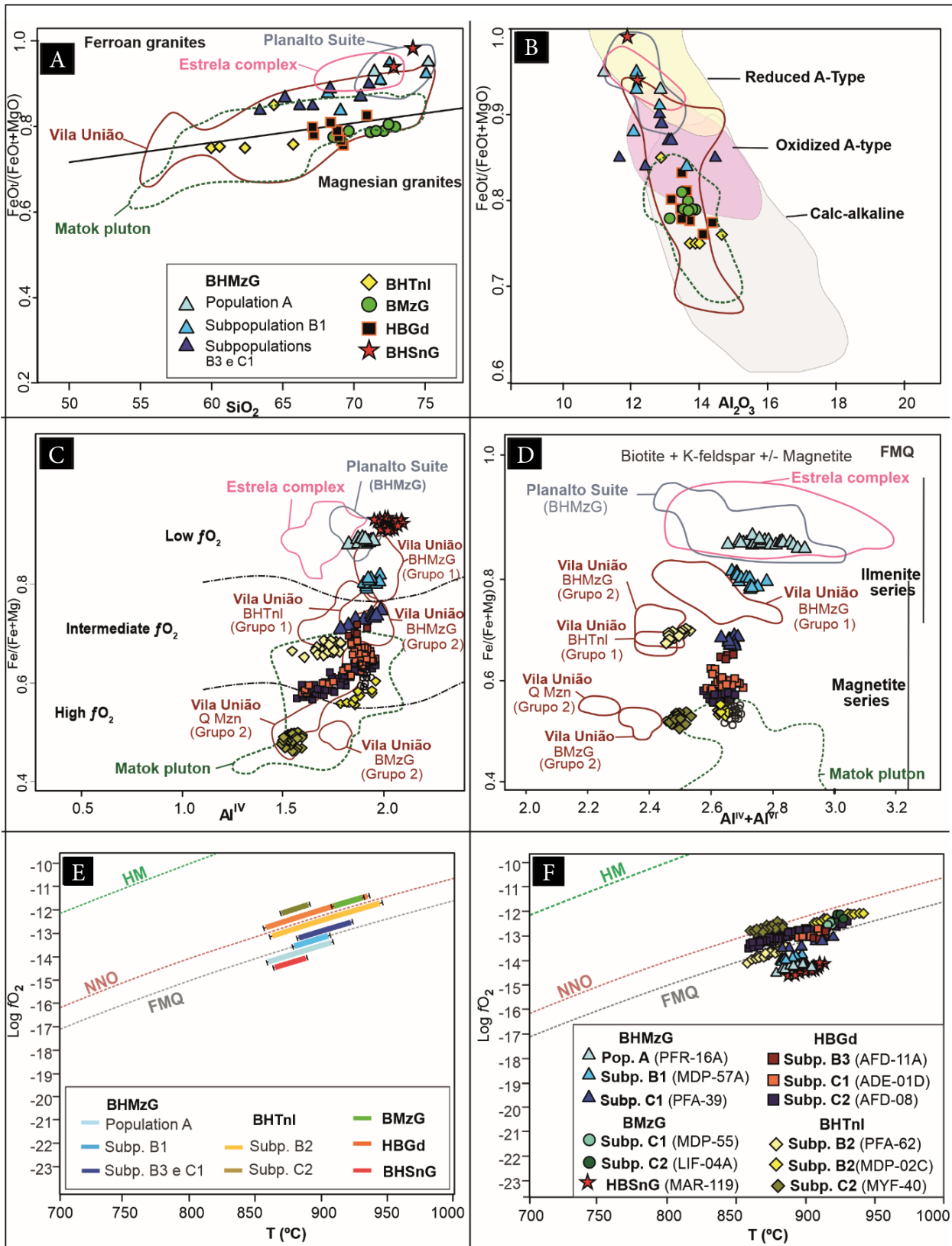
Subp: subpopulation; Pop: population; B: biotite; H: hornblende; SnG: syenogranite; Mzg: monzogranite; Gd: granodiorite; Tnl: tonalite; Q Mzn: quartz-monzonite.

Figure 12. (A) SiO₂ vs. FeOt/(FeOt + MgO) and (B) FeOt/(FeOt + MgO) vs. Al₂O₃ diagrams of the VJS showing, respectively, the fields of Frost *et al.* (2001) and those of reduced and oxidized A-type granites and calc-alkaline Cordilleran granitoids (Dall'Agnol and Oliveira 2007); (C) Fe/(Fe + Mg) vs Al^{IV} diagram in amphiboles of different varieties of the VJS showing the behavior of the rocks regarding fO₂ (low-, intermediate- and high-fO₂ fields according to Anderson and Smith 1995); (D) Fe/(Fe + Mg) vs Al^{IV} + Al^{VI} diagram showing the biotite composition of different varieties from the VJS. Biotite compositional variations of granites of the magnetite and ilmenite series (Ishihara 1981) according to Anderson *et al.* (2008). (E) T versus log$f$O₂ diagram showing ranges of temperature and fugacity conditions (fO₂) empirically estimated for different varieties of VJS granitoids; (F) Temperature versus log$f$O₂ diagram for the VJS granitoids, with the temperatures and fO₂ calculated based on the amphibole composition according to Ridolfi *et al.* (2010). Fayalite-magnetite-quartz (FMQ) and nickel-nickel oxide (NNO) buffer curves according to Frost (1991). In Figs. 12A, 12B, 12C, and 12D, the fields of Planalto suite, Estrela Complex, Vila União granitoids, and Matok pluton are shown for comparison (see references in the text).

show that it crystallized under oxidizing conditions estimated to be close to NNO+0.5 (Fig. 12E).

Lastly, the BHSnG variety shows a contradictory behavior, as highlighted earlier. This variety has high opaque modal content, is enriched in magnetite, and displays maximum values of MS (Tab. 3, Suppl. Tab. A4). However, it shows the highest value of whole rock FeOt/(FeOt + MgO) ratios and should be classified as a reduced A-type granite (Figs. 12A and 12B).

Experimental studies demonstrated the existence of a close relationship between fO_2 and the Mg* parameter of amphibole (Scaillet and Evans 1999, Ridolfi et al. 2008, 2010). To assess the consistency of empirical fO_2 values estimated for different varieties of the VJS, the log fO_2 values were calculated based on amphibole composition using Eq. 1, by Ridolfi et al. (2010):

$$\Delta NNO = 1.644 \ Mg^* - 4.01 \tag{1}$$

Where:
$Mg^* = Mg + Si/47 - {}^{[6]}Al/9 - 1.3 {}^{[6]}Ti + Fe^{3+}/3.7 + Fe^{2+}/5.2 - {}^{B}Ca/20 - {}^{A}Na/2.8 + {}^{A}[]/9.5$

This equation has an estimated precision of 0.22 units of log fO_2 (Ridolfi et al. 2010), which is consistent with the uncertainty of other experimental studies (0.2-0.3 units of log fO_2; Scaillet and Evans 1999, Pichavant et al. 2002). Erdmann et al. (2014) consider the fO_2 estimates of Ridolfi et al. (2010) to be consistent with experimental results available in the literature.

The detected mean values for temperature and fO_2 according to Ridolfi et al. (2010) for the different samples studied are shown in Fig. 12F. The standard deviation of these values in different samples is systematically low and the values obtained in the different analyses are also represented to indicate the variability in each sample.

The model by Ridolfi et al. (2010) indicates fO_2 values for the granites studied (Fig. 12F) that generally approach those estimated by our empirical method. It is concluded that the values estimated by the empirical approach and the values determined via the amphibole composition using the method by Ridolfi et al. (2010) are consistent in the sense that the estimated or calculated fO_2 values show a similar trend in the different granite varieties. However, they differ by the fact that the fO_2 deduced by the Ridolfi et al. (2010) method is one unit or half unit of log fO_2 below those estimated by the empirical approach (Figs. 12E and 12F).

We consider that the model of Ridolfi et al. (2010) is generally suitable for the estimation of fO_2 (cf. Erdmann et al. 2014) and that our empirical estimates also provide reasonable fO_2 values. The observed differences between both methods in the VJS are possibly because Ridolfi et al. (2010) based their oxybarometer in experimental studies of magnesian calc-alkaline rocks with Fe/(Fe + Mg) in amphibole lower than those observed in the VJS.

Based on our empirical estimation, it is concluded that the granites studied display fO_2 varying from reduced to oxidized, corresponding to conditions below FMQ to NNO+1. The reduced and oxidized ferroan BHMzG crystallized at fO_2 conditions corresponding to < FMQ to FMQ+0.5 and

the magnesian BHTnl, BMzG, and HBGd at NNO-0.5 to NNO+1. The estimates based on Ridolfi et al. (2010) yield comparatively slightly lower fO_2 values.

The paradoxical behavior observed in the BHSnG group is not easy to explain. It is known that the occurrence of magnetite in granites does not imply necessarily oxidizing conditions (Anderson and Morrison 2005, Dall'Agnol and Oliveira 2007) because granitic rocks crystallizing at FMQ should contain magnetite and are considered to be reduced rocks. However, the high modal content of opaque minerals and the total dominance of magnetite in the BHSnG require further investigation. A possible alternative would be to assume that magnetite is a phase that formed independently of the liquid generating this granite and has a cumulate origin or was generated at levels of fluid flow, although there is no conclusive evidence to support these hypotheses.

Comparisons between the Vila Jussara Suite and similar Archean granitoids

The data obtained in the VJS were compared with that of the Neoarchean granites of the Planalto Suite (Cunha et al. 2016), Estrela Complex (Barros et al. 2001), and Vila União granitoids (Oliveira et al. 2018), all of the CP, and Neoarchean granitoids of the Matok pluton (Rapopo 2010, Laurent et al. 2014), which is located in the Limpopo Belt, South Africa.

The reduced ferroan BHMzG of population A and sub-population B_1 are similar to the Planalto Suite and Estrela Complex granites and the oxidized ferroan BHMzG of sub-populations B_3 and C_1 are more akin to part of the granitoids of the Vila União area (Figs. 12A and 12B). The BHTnl, BMzG, and HBGd of the VJS are all magnesian granitoids and show similar geochemical behavior. The BHMzG are clearly distinct in terms of the composition of the magnesian granitoids of the VJS and Vila União area, as well as of the magnesian Matok pluton granitoids (Figs. 12A and 12B). The Serra do Rabo granite (Sardinha et al. 2006) and the Igarapé Gelado granite (Barros et al. 2009), both of the CP, and not represented in the diagrams, are composed, respectively, of reduced ferroan granites and varying from reduced to oxidized ferroan granitoids.

A similar picture is given by the variation of Fe/(Fe + Mg) in amphibole and biotite (Figs. 12C and 12D), which indicates low fO_2 for the reduced granites of the VJS, Planalto Suite, Estrela complex, and part of Vila União granites, passing to intermediate in the oxidized ferroan BHMzG of the VJS and Vila União. In the magnesian granitoids of the VJS, Vila União, and Matok, the fO_2 values are higher than in the reduced and oxidized ferroan granites and increase gradually from intermediate to high (Fig. 12C). The biotite composition is similar to that of biotite of ilmenite series granites in the reduced granites and is comparable to that of magnetite series granites in the oxidized ferroan and magnesian granitoids (Fig. 12D), attaining minimum Fe/(Fe+Mg) values in the Matok pluton, suggesting that it can have a more oxidized character, compared with the VJS granitoids.

It is concluded that whole rock and mineral chemistry data are consistent and demonstrate that the fO_2 behavior observed in the VJS is also found in other similar Neoarchean granites

of the CP. The granitoids of the Matok pluton approach the magnesian granitoids of the CP.

Possible causes for oxygen fugacity variation in the Vila Jussara Suite granitoids

Most granitic magmas tend to have a pattern and align with a buffer during their evolution (Dall'Agnol *et al.* 2005, Cunha *et al.* 2016). However, Loucks *et al.* (2018) showed evidence that several magmatic suites follow fO_2 trends that are not parallel to the buffer curves. They argued that poor-water magmas tend to show a relative decrease in fO_2, whereas water-rich magmas, such as those of the VJS (*cf.* Dall'Agnol *et al.* 2017), could display increasing fO_2 trends.

Among other possible explanations for variations of fO_2 in the VJS, the following two reasons are highlighted.

- Compositional variations in magma source resulted in fO_2 contrasts in the generated liquid: this hypothesis was initially postulated by Dall'Agnol *et al.* (2017), who argued that the reduced varieties of the VJS and other Neoarchean granites would be related to metamorphosed, reduced, tholeiitic sources in granulite facies, whereas oxidized sources would be related to calc-alkaline mafic to intermediate granulites. This hypothesis remains valid and assumes that the reduced or oxidized character of the magmas of Neoarchean granitoids would be essentially a feature inherited from the magma source (*cf.* Carmichael 1991, Frost and Frost 1997, Pichavant *et al.* 1996, Rajesh 2008);

- Presence in the magmatic liquid of volatile constituents which may cause variations in the fO_2 of magma during its crystallization. In this hypothesis, a mineralogical feature of the Vila Jussara granitoids stands out. The most markedly reduced varieties (BHMzG from population A and subpopulation B_1) have virtually no pyrite or other types of sulfides and the latter starts to occur significantly in the moderately oxidized BHMzG of subpopulations B_3 and C_1 (Tab. 3, Suppl. Tab. A1). In the other varieties of the VJS, which include only oxidized magnesian granitoids, the sulfides are the most abundant modal opaque phase in the biotite-hornblende tonalites (Tab. 3, Suppl. Tab. A2) and immediately follow magnetite in abundance in the biotite monzogranites and hornblende-biotite granodiorites groups (Tab. 3, Suppl. Tabs. A3 and A4). Reduced granites of the Planalto Suite (Cunha *et al.* 2016) show the same type of features as those described in the reduced varieties of the VJS.

Moussallam *et al.* (2014) discussed the possible effect of sulfur on variations in the degree of oxidation of magmas in volcanic environments. They showed evidence that the release of sulfur-rich volatiles by degasification affects the fO_2 of residual liquids, which tend to be more reduced. By extension, we can assume that the presence of significant amounts of sulfides in the magma, as indicated by the occurrence of pyrite, may have caused oxidation, which would explain the contrast in the degree of oxidation between the oxidized pyrite-bearing granitoids and the reduced granitoids devoid of pyrite and, as a consequence, of sulfur in appreciable amounts.

Another volatile component that could affect the fO_2 in magma is water. Gaillard *et al.* (2001) experimentally assessed the effects of adding water to liquids in terms of variations in fO_2, and they concluded that water can have an oxidizing effect (*cf.* Loucks *et al.* 2018). However, this effect is restricted to relatively reduced magmatic liquids, and the presence of dissolved water in oxidized calc-alkaline magmas should not exert a marked effect on fO_2. These observations may help to explain the variation in fO_2 between the granites of groups 1 and 2 of the Planalto Suite and, by analogy, between the BHMzG of population A and subpopulation B_1 of the VJS. The slight contrast in fO_2 between these rocks may reflect a comparative increase in the water content of rocks containing magnetite, which are somewhat more oxidized than those devoid of magnetite.

The hypotheses outlined here can be effective in different situations, either alone or combined. However, at the present stage, we cannot provide conclusive evidence about the causes of variations in fO_2 in the granitoids of the VJS.

CONCLUSIONS

The granitoids of the VJS were divided into four main petrographic groups with wide variation in magnetic behavior.

The BHMzG group is formed by two subgroups: the first group consists of reduced ferroan granites derived from magma, whose fO_2 evolved from lower than FMQ to equal to or slightly higher than FMQ. The second subgroup includes oxidized ferroan granites that evolved under conditions above the FMQ buffer but below the NNO buffer (FMQ+0.5).

The BHTnl variety includes magnesian granitoids that evolved under essentially oxidizing conditions, with the dominant set formed under conditions equivalent to NNO-0.5 to NNO, although sample MYF-40 is near NNO+1. The BMzG and HBGd groups include granitoids of the magnetite series that are geochemically similar to magnesian granites and crystallized under oxidizing conditions (NNO to NNO-0.5).

In addition to the aforementioned groups, the BHSnG was formed, presumably, under strongly reduced conditions, although a conclusive explanation for its high magnetite content was not determined.

The indicated fO_2 values were obtained with our empirical estimations. They approach those indicated by the experimental method of Ridolfi *et al.* (2010) showing a reasonable correspondence between these two methods.

Subgroup 1 of the VJS BHMzG is quite similar to the granites of the Planalto Suite, Estrela complex, and the reduced ferroan granitoids of Vila União, which evolved under reducing conditions (FMQ ± 0.5). The other varieties of the VJS, BHTnl, BMzG, and HBGd, were formed under essentially oxidizing conditions and, in this regard, are similar to the oxidized granites of Vila União, which both crystallized under moderate to high fO_2 conditions (from NNO ± 0.5 to NNO + 1). In general, the Neoarchean granitoids of the Matok Pluton of Limpopo Belt, South Africa, approach, in terms of degree of oxidation, the magnesian granitoids of the VJS rocks, but they tend to exhibit a more oxidized character.

ACKNOWLEDGEMENTS

ARTICLE INFORMATION

REFERENCES

Almeida J.A.C., Dall'Agnol R., Leite A.A.S. 2013. Geochemistry and zircon geochronology of the Archean granite suites of the Rio Maria granite-greenstone terrane, Carajás Province, Brazil. *Journal of South American Earth Sciences*, **42**:103-126. https://doi.org/10.1016/j.jsames.2012.10.008

Almeida J.A.C., Dall'Agnol R., Oliveira M.A., Macambira M.B., Pimentel M.M., Rämö O.T., Guimarães F.V., Leite A.A.S. 2011. Zircon geochronology and origin of the TTG suites of the Rio Maria granite-greenstone terrane: Implications for the growth of the Archean crust of the Carajás province, Brazil. *Precambrian Research*, **187**(1-2):201-221. https://doi.org/10.1016/j.precamres.2011.03.004

Althoff F.J., Barbey P., Boullier A.M. 2000. 2.8-3.0 Ga plutonism and deformation in the SE Amazonian craton: the Archean granitoids of Marajoara (Carajás Mineral Province, Brazil). *Precambrian Research*, **104**(3-4):187-206. https://doi.org/10.1016/S0301-9268(00)00103-0

Anderson J.L., Barth A.P., Wooden J.L., Mazdab F. 2008. Thermometers and thermobarometers in granitic systems. *Reviews in Mineralogy and Geochemstry*, **69**(1):121-142. https://doi.org/10.2138/rmg.2008.69.4

Anderson, J.L., Morrison, J., 2005. Ilmenite, magnetite and peraluminous Mesoproterozoic anorogenic granites of Laurentia and Baltica. *Lithos*, **80**(1-4):45-60. https://doi.org/10.1016/j.lithos.2004.05.008

Anderson J.L., Smith D.R. 1995. The effects of temperature and fO_2 on the Al-in-hornblende barometer. *American Mineralogist*, **80**(5-6):549-559. https://doi.org/10.2138/am-1995-5-614

Arató R., Audétat A. 2017. Vanadium magnetite–melt oxybarometry of natural, silicic magmas: a comparison of various oxybarometers and thermometers. *Contributions to Mineralogy and Petrology*, **172**:52. https://doi.org/10.1007/s00410-017-1369-6

Armstrong J.T. 1995. CITZAF: a package of correction programs for the quantitative electron microbeam X-ray analysis of thick polished materials, thin films, and particles. *Microbeam Analysis*, **4**:177-200.

Barbosa J.P.O. 2004. *Geologia estrutural, geoquímica, petrografia e geocronologia de granitoides da região do Igarapé Gelado, norte da Província Mineral de Carajás*. Dissertação de Mestrado, Programa de Pós-graduação em Geologia e Geoquímica, Instituto de Geociências, Universidade Federal do Pará, Belém, 96 p.

Barros C.E.M., Barbey P., Boullier A.M. 2001. Role of magma pressure, tectonic stress and crystallization progress in the emplacement of the syntectonic A-type Estrela Granite Complex (Carajás Mineral Province, Brazil). *Tectonophysics*, **343**(1-2):93-109. https://doi.org/10.1016/S0040-1951(01)00260-8

Barros C.E.M., Sardinha A.S., Barbosa J.P.O., Macambira M.J.B. 2009. Structure, petrology, geochemistry and zircon U/Pb and Pb/Pb geochronology of the synkinematic Archean (2.7 Ga) A-Type granites from the Carajás Metallogenic Province, northern Brazil. *Canadian Mineralogist*, **47**:1423-1440.

Buddington A.F., Lindsley D.H. 1964. Iron-titanium oxide minerals and synthetic equivalents. *Journal of Petrology*, **5**(2):310-357. https://doi.org/10.1093/petrology/5.2.310

Carmichael I.S.E. 1991. The redox states of basic and silicic magmas: a reflection of their source regions. *Contributions to Mineralogy and Petrology*, **106**:129-141. https://doi.org/10.1007/BF00306429

Chakraborti T.M., Ray A., Deb G.K., Upadhyay D., Chakrabarti R. 2019. Evidence of crustal reworking in the Mesoarchean: Insights from geochemical, U-Pb zircon and Nd isotopic study of a 3.08–3.12 Ga ferro-potassic granite-gneiss from north-eastern margin of Singhbhum Craton, India. *Lithos*, **330-331**:16-34. https://doi.org/10.1016/j.lithos.2019.01.026

Clark D.A. 1999. Magnetic petrology of igneous intrusions: implications for exploration and magnetic interpretation. *Exploration Geophysics*, **30**:5-26.

Cunha I.R.V., Dall'Agnol R., Feio G.R.L. 2016. Mineral chemistry and magnetic petrology of the Archean Planalto Suite, Carajás Province - Amazonian Craton: Implications for the evolution of ferroan Archean granites. *Journal of South American Earth Sciences*, **67**:100-121. https://doi.org/10.1016/j.jsames.2016.01.007

Cunha I.R.V., Dall'Agnol R., Scaillet B., Sousa L.A.M. 2021. Magmatic epidote in Archean granitoids of the Carajás province, Amazonian craton, and its stability during magma rise and emplacement. *Journal of South American Earth Sciences*, **112**(Part 1):103570. https://doi.org/10.1016/j.jsames.2021.103570

Czamanske G.K., Mihalik P. 1972. Oxidation during magmatic differentiation, Finnmarka complex, Oslo area, Norway: Part 1, The opaque oxides. *Journal of Petrology*, **13**(3):493-509. https://doi.org/10.1093/petrology/13.3.493

Dall'Agnol R., Cunha I.R.V., Guimarães F.V., Oliveira D.C., Teixeira M.F.B., Feio G.R.L., Lamarão C.N. 2017. Mineralogy, geochemistry, and petrology of Neoarchean ferroan to magnesian granites of Carajás Province, Amazonian Craton: The origin of hydrated granites associated with charnockites. *Lithos*, **277**:3-32. https://doi.org/10.1016/j.lithos.2016.09.032

Dall'Agnol R., Oliveira D.C. 2007. Oxidized, magnetite series, rapakivi-type granites of Carajás, Brazil: implications for classification and petrogenesis of A-type granites. *Lithos*, **93**(3-4):215-233. https://doi.org/10.1016/j.lithos.2006.03.065

Dall'Agnol R., Oliveira D.C., Guimarães F.V., Gabriel E.O., Feio G.R.L., Lamarão C.N., Althoff F.A., Santos P.A., Teixeira M.F.B., Silva A.C., Rodrigues D.S., Santos C.R.P., Silva R.D., Santos P.J.L. 2013. Geologia do Subdomínio de Transição do Domínio Carajás – implicações para a evolução arqueana da Província Carajás – Pará. *In*: Simpósio de Geologia da Amazônia, 13. *Anais...* 1 CD-ROM.

Dall'Agnol R., Oliveira M.A., Almeida J.A.C., Althoff F.J., Leite A.A.S., Oliveira D.C., Barros, C.E.M. 2006. Archean and Paleoproterozoic granitoids of the Carajás metallogenic province, eastern Amazonian craton. *In*: Dall'agnol R., Rosa-Costa L.T., Klein E.L. (eds.). *Symposium on Magmatism, Crustal Evolution, and Metallogenesis of the Amazonian Craton.* Abstracts Volume and Field Trips Guide. Belém: PRONEX-UFPA/SBG-NO, 150 p.

Dall'Agnol R., Pichavant M., Champenois M. 1997. Iron-titanium oxide minerals of the Jamon Granite, eastern Amazonian region, Brazil: implications for the oxygen fugacity in Proterozoic, A-type granites. *Anais da Academia Brasileira de Ciências*, **69**(3):325-347.

Dall'Agnol R., Teixeira N.P., Ramo O.T., Moura C.A.V., Macambira M.J.B., Oliveira D.C. 2005. Petrogenesis of the Paleoproterozoic, rapakivi, A-type granites of the Archean Carajás Metallogenic Province, Brazil. *Lithos*, **80**(1-4):101-129. https://doi.org/10.1016/j.lithos.2004.03.058

Deer W.A., Howie R.A., Zussman J. 2013. *An introduction to the rock forming minerals*. 3. ed. United Kingdom: Geology Society of London, 505 p.

Erdmann S., Martel C., Pichavant M., Kushnir A. 2014. Amphibole as an archivist of magmatic crystallization conditions: problems, potential, and implications for inferring magma storage prior to the paroxysmal 2010 eruption of Mount Merapi, Indonesia. *Contributions to Mineralogy and Petrology*, **167**:1016. https://doi.org/10.1007/s00410-014-1016-4

Feio GRL., Dall'Agnol R. 2012. Geochemistry and petrogenesis of the Mesoarchean granites from the Canaã dos Carajás Area, Carajás Province, Brazil: implications for the origin of Archean granites. *Lithos*, **154**:33-52. https://doi.org/10.1016/j.lithos.2012.06.022

Feio G.R.L., Dall'Agnol R., Dantas E.L., Macambira M.J.B., Gomes A.C.B., Sardinha A.S., Santos P. 2012. Geochemistry, geochronology, and origin of the Planalto granite suite and associated rocks: implications for the Neoarchean evolution of the Carajás Province. *Lithos*, **151**:57-73. https://doi.org/10.1016/j.lithos.2012.02.020

Feio G.R.L., Dall'Agnol R., Dantas E.L., Macambira M.J.B., Santos J.O.S., Althoff F.J. 2013. Archean granitoid magmatism in the Canaã dos Carajás area: Implication for crustal evolution of the Carajás province, Amazonian craton, Brazil. *Precambrian Research*, **227**:157-185. https://doi.org/10.1016/j.precamres.2012.04.007

Frost B.R. 1991. Magnetic petrology: factors that control the occurrence of magnetite in crustal rocks. *In*: Lindsley D.H. (ed.). *Oxide minerals:* petrologic and magnetic significance. Mineralogy Society of America, Reviews in Mineralogy, **25**:489-509.

Frost B.R., Barnes C.G., Collins W.J., Arculus R.J., Ellis D.J., Frost C.D. 2001. A geochemical classification for granitic rocks. *Journal of Petrology*, **42**(11):2033-2048. https://doi.org/10.1093/petrology/42.11.2033

Frost B.R., Lindsley D.H. 1992. Equilibria among Fe-Ti oxides, pyroxenes, olivine, and quartz: Part II. Application. *American Mineralogist*, **77**(9-10):1004-1020.

Frost C.D., Frost B.R. 1997. Reduced rapakivi type granites: the tholeiitic connection. *Geology*, **25**(7):647-650. https://doi.org/10.1130/0091-7613(1997)025%3C0647:RRTGTT%3E2.3.CO;2

Gabriel E.O. 2014. Geologia, petrografia e geoquímica dos granitoides arqueanos de alto magnésio da região de Água Azul do Norte, porção sul do Domínio Carajás, Pará. *Boletim do Museu Paraense Emilio Goeldi Ciências Naturais*, **9**(3):533-564.https://doi.org/10.46357/bcnaturais.v9i3.509

Gaillard F., Scaillet B., Pichavant M., Bény J.M. 2001. The effect of water and fO$_2$ on the ferric–ferrous ratio of silicic melts. *Chemical Geology*, **174**(1-3):255-273. https://doi.org/10.1016/S0009-2541(00)00319-3

Geuna S.E., McEnroe S.A., Robinson P., Escosteguy L.D. 2008. Magnetic petrology of the Devonian Achala Batholith, Argentina: Titanohaematite as an indicator of highly oxidized magma during crystallization and cooling. *Geophysical Journal International*, **175**(3):925-941. https://doi.org/10.1111/j.1365-246X.2008.03964.x

Ghiorso M.S., Evans B.W. 2008. Thermodynamics of rhombohedral oxide solid solutions and a revision of the Fe-Ti two-oxide geothermometer and oxygen-barometer. *American Journal of Science*, **308**(9):957-1039. https://doi.org/10.2475/09.2008.01

Haggerty S.E. 1991. Oxide textures: a mini-atlas. *In*: Lindsley D.H. (ed.). *Oxide minerals:* petrologic and magnetic significance. Mineralogy Society of America, Reviews in Mineralogy, **25**:129-219.

Hawthorne F.C., Oberti R., Harlow G.E., Maresch W.V., Martin R.F., Schumacher J.C., Welch M. 2012. IMA Report – Nomenclature of the amphibole supergroup. *American Mineralogist*, **97**(11-12):2031-2048. https://doi.org/10.2138/am.2012.4276

Huhn S.B., Macambira M.J.B., Dall'Agnol R. 1999. Geologia e geocronologia Pb/Pb do granito alcalino arqueano planalto, região da Serra do Rabo, Carajás-PA. *In*: Simpósio de Geologia da Amazônia, 6., Manaus. *Boletim de Resumos Expandidos*. Manaus: SBG-NNO, **1**:463-466.

Ishihara S. 1977. The magnetite-series and ilmenite-series granitic rocks. *Mining Geology*, **27**(145):293-305. https://doi.org/10.11456/shigenchishitsu1951.27.293

Ishihara S. 1981. The granitoid series and mineralization. *Economic Geology*, **75**:458-484. https://doi.org/10.5382/AV75.14

Janoušek V., Farrow C.M., Erban V. 2006. Interpretation of whole-rock geochemical data in igneous geochemistry: introducing Geochemical Data Toolkit (GCDkit). *Journal of Petrology*, **47**(6):1255-1259. https://doi.org/10.1093/petrology/egl013

Javier Rios F., Villas R.N., Dall'Agnol R. 1995. O Granito Serra dos Carajás: fácies petrográficas e avaliação do potencial metalogenético para estanho no setor norte. *Revista Brasileira de Geociências*, **25**:20-31.

Jayananda M., Chardon D., Peucat J.J., Capdevila R. 2006. 2.61 Ga potassic granites and crustal reworking in the western Dharwar craton, southern India: tectonic, geochronologic and geochemical constraints. *Precambrian Research*, **150**(1-2):1-26. https://doi.org/10.1016/j.precamres.2006.05.004

Laurent O., Rapopo M., Stevens G., Moyen J.F., Martin H., Doucelance R., Bosq C. 2014. Contrasting petrogenesis of MgeK and FeeK granitoids and implications for post- colisional magmatism: case study from the Late-Archean Matok pluton (Pietersburg block, South Africa). *Lithos*, **196-197**:131-149. https://doi.org/10.1016/j.lithos.2014.03.006

Leite-Santos P.J.L., Oliveira D.C. 2016. Geologia, petrografia e geoquímica das associações leucograníticas arqueanas da área de Nova Canadá – Província Carajás. *Geologia USP, Série Científica*, **16**(2):37-66.

Le Maitre R.W., Streckeisen A., Zanettin B., Le Bas M.J., Bonin P., Bateman P., Bellieni G., Dudek A., Efremova S., Keller J., Lameyre J., Sabine P.A., Schmid R., Sørensen H., Woolley A.R. 2002. Igneous rocks: a classification and glossary of terms. Recommendations of the International Union of Geological Sciences (IUGS), Subcommission on the Systematics of Igneous Rocks. 2. ed. Cambridge: Cambridge University Press, 236 p.

Loucks R.R., Fiorentini M.L., Rohrlach B.D. 2018. Divergent T–fO_2 paths during crystallisation of H$_2$O-rich and H$_2$O-poor magmas as recorded by Ce and U in zircon, with implications for TitaniQ and TitaniZ geothermometry. *Contributions to Mineralogy and Petrology*, **173**(12):104. https://doi.org/10.1007/s00410-018-1529-3

Macambira M.J.B., Lancelot J. 1996. Time constraints for the formation of the Archean Rio Maria crust, southeastern Amazonian Craton, Brazil. *International Geology Review*, **38**(12):1134-1142. https://doi.org/10.1080/00206819709465386

Machado N., Lindenmayer Z., Krogh T.H., Lindenmayer Z.G. 1991. U-Pb geochronology of Archaean magmatism and basement reactivation in the Carajás area, Amazon shield, Brazil. *Precambrian Research*, **49**(3-4):329-354. https://doi.org/10.1016/0301-9268(91)90040-H

Magalhães M.S., Dall'Agnol R., Sauck W.A., Gouvea L.J. 1994. Suscetibilidade magnética: um indicador da evolução petrológica de granitoides da Amazônia. *Revista Brasileira de Geociências*, **24**(3):139-149.

Marangoanha B., Oliveira D.C., Oliveira V.E.S., Galarza M.A., Lamarão C.N. 2019. Neoarchean A-type granitoids from Carajás province (Brazil): New insights from geochemistry, geochronology and microstructural analysis. *Precambrian Research*, **324**:86-108. https://doi.org/10.1016/j.precamres.2019.01.010

Martin H., Smithies R.H., Rapp R., Moyen J.F., Champion D. 2005. An overview of adakite, tonalite-trondhjemite-granodiorite (TTG) and sanukitoid: relationships and some implications for crustal evolution. *Lithos*, **79**(1-2):1-24. https://doi.org/10.1016/j.lithos.2004.04.048

Martins P.L.G., Toledo C.L.B., Silva A.M., Chemale F., Santos J.O.S., Assis L.M. 2017. Neoarchean magmatism in the southeastern Amazonian Craton, Brazil: Petrography, geochemistry and tectonic significance of basalts from the Carajás Basin. *Precambrian Research*, **302**:340-357. https://doi.org/10.1016/j.precamres.2017.10.013

Mesquita C.J.S., Dall'Agnol R., Almeida J.A.C. 2018. Mineral chemistry and crystallization parameters of the A-type Paleoproterozoic Bannach Granite, Carajás Province, Pará, Brazil. *Brazilian Journal of Geology*, **48**(3):575-601. https://doi.org/10.1590/2317-4889201820170082

Moreto C.P.N., Monteiro L.V.S., Xavier R.P., Amaral W.S., Santos T.J.S., Juliani C., Souza Filho C.R. 2011. Mesoarchean (3.0 and 2.86 Ga) host rocks of the iron oxide e Cu e Au Bacaba deposit, Carajas Mineral Province: U e Pb geochronology and metallogenetic implications, *Mineralium Deposita*, **46**(7):789-811. https://www.doi.org/10.1007/s00126-011-0352-9

Morgan G.B., London D. 2005. Effect of current density on the electron microprobe analysis of alkali aluminosilicate glasses. *American Mineralogist*, **90**(7):1131-1138. https://doi.org/10.2138/am.2005.1769

Moussallam Y., Oppenheimer C., Scaillet B., Gaillard F., Kyle P., Peters N., Hartley M., Berlo, K., Donovan A. 2014. Tracking the changing oxidation state of Erebus magmas, from mantle to surface, driven by magma ascent and degassing. *Earth and Planetary Science Letters*, **393**:200-209. https://doi.org/10.1016/j.epsl.2014.02.055

Moyen J.F., Laurent O. 2018. Archaean tectonic systems: A view from igneous rocks. *Lithos*, **302-303**:99-125. https://doi.org/10.1016/j.lithos.2017.11.038

Oliveira C.G., Leonardos O.H. 1990. Gold mineralization in the Diadema shear belt, northern Brazil. *Economic Geology*, **85**(5):1034-1043. https://doi.org/10.2113/gsecongeo.85.5.1034

Oliveira D.C., Dall'Agnol R., Silva J.B.C., Almeida J.A.C. 2008. Gravimetric, radiometric, and magnetic susceptibility study of the Paleoproterozoic Redenção and Bannach plutons, eastern Amazonian Craton, Brazil: Implications for architecture and zoning of A-type granites. *Journal of South American Earth Sciences*, **25**(1):100-115. https://doi.org/10.1016/j.jsames.2007.10.003

Oliveira M.A., Dall'Agnol R., Almeida J.A.C. 2011. Petrology of the Mesoarchean Rio Maria suite and the discrimination of sanukitoid series. *Lithos*, **127**(1-2):192-209. https://doi.org/10.1016/j.lithos.2011.08.017

Oliveira M.A., Dall'Agnol R., Althoff F.J., Leite A.A.S. 2009. Mesoarchean sanukitoid rocks of the Rio Maria Granite-Greenstone Terrane, Amazonian craton, Brazil. *Journal of South American Earth Sciences*, **27**(2-3):146-160. https://doi.org/10.1016/j.jsames.2008.07.003

Oliveira M.A., Dall'Agnol R., Scaillet B. 2010. Petrological constraints on crystallization conditions of Mesoarchean sanukitoid rocks, southeastern Amazonian craton, Brazil. *Journal of Petrology*, **51**(10):2121-2148. https://doi.org/10.1093/petrology/egq051

Oliveira D.C., Leite-Santos P.J., Gabriel E.O., Rodrigues D.S., Faresin A.C., Silva M.L.T., Sousa S.D., Santos R.V., Silva A.C., Souza M.C., Santos R.D., Macambira M.J.B. 2010. Aspectos geológicos e geocronológicos das rochas magmáticas e metamórficas da região entre os municípios de Água Azul do Norte e Canaã dos Carajás Província Mineral de Carajás. *In*: Congresso Brasileiro de Geologia, 45. *Anais...* Salvador: SBG. CD-ROM.

Oliveira V.E.S., Oliveira D.C., Marangoanha B., Lamarão C.N. 2018. Geology, mineralogy and petrological affinities of the Neoarchean granitoids from the central portion of the Canaã dos Carajás domain, Amazonian craton, Brazil. *Journal of South American Earth Sciences*, **85**:135-159. https://doi.org/10.1016/j.jsames.2018.04.022

Papike J.J. 1987. Chemistry of the rock-forming silicates: Ortho, ring, and single-chain structures. *Reviews of Geophysics*, **25**(7):1483-1526. https://doi.org/10.1029/RG025i007p01483

Papike J.J. 1988. Chemistry of the rock-forming silicates: Multiple-chain, sheet, and framework structures. *Reviews of Geophysics*, **26**(3):407-444. https://doi.org/10.1029/RG026i003p00407

Pichavant M., Hammouda T., Scaillet B. 1996. Control of redox state and Sr isotopic composition of granitic magmas: a critical evaluation of the role of source rocks. *Transactions of the Royal Society of Edinburgh: Earth Science*, **87**(1-2):321-329. https://doi.org/10.1017/S0263593300006714

Pichavant M., Martel C., Bourdier J.L., Scaillet B. 2002. Physical conditions, structure, and dynamics of a zoned magma chamber: Mount Pelee (Martinique, Lesser Antilles Arc). *Journal Geophysics Research*, **107**(B5): ECV1-28. https://doi.org/10.1029/2001JB000315

Putirka K. 2016. Rates and styles of planetary cooling on Earth, Moon, Mars, and Vesta, using new models for oxygen fugacity, ferric-ferrous ratios, olivine-liquid Fe–Mg exchange, and mantle potential temperature. *American Mineralogist*, **101**(4):819-840. https://doi.org/10.2138/am-2016-5402

Rapopo M. 2010. *Petrogenesis of the Matok Pluton, South Africa: implications on the heat source that induced regional metamorphism in the southern marginal zone of the Limpopo Belt*. Master Thesis, University of Stellenbosch, South Africa, 197 p.

Rahaman M.S., Mondal M.E.A., Ahmad I., Bhutani R., Choudhary A.K. 2019. Geochemical and Nd isotopic studies of the Neoarchaean-Palaeoproterozoic granitoids of the Aravalli Craton, NW India: evidence for heterogeneous crustal evolution processes. *In*: Mondal M.E.A. (ed.). *Geological evolution of the Precambrian Indian Shield*. Berlin-Heidelberg: Springer, p. 327-350.

Rajesh H.M. 2008. Petrogenesis of two granites from the Nilgiri and Madurai blocks, southwestern India: Implications for charnockite–calc-alkaline granite and charnockite–alkali (A-type) granite link in high-grade terrains. *Precambrian Research*, **162**(1-2):180-197. https://doi.org/10.1016/j.precamres.2007.07.023

Ridolfi F., Puerini M., Renzulli A., Menna M., Toulkeridis T. 2008. The magmatic feeding system of El Reventador volcano (Sub-Andean zone, Ecuador) constrained by texture, mineralogy and thermobarometry of the 2002 erupted products. *Journal of Volcanology and Geothermal Research*, **176**(1):94-106. https://doi.org/10.1016/j.jvolgeores.2008.03.003

Ridolfi F., Renzulli A., Puerini M. 2010. Stability and chemical equilibrium of amphibole in calc-alkaline magmas: an overview, new thermobarometric formulations, and application to subduction-related volcanoes. *Contributions to Mineralogy and Petrology*, **160**:45-66. https://doi.org/10.1007/s00410-009-0465-7

Rieder M., Cavazzini G., D'yakonov Y.S., Frank-Kamenetskii V.A., Gottardi G., Guggenheim S., Koval P.V., Müller G., Neiva A.M.R., Radoslovich E.W., Robert J.L., Sassi F.P., Takeda H., Weiss Z., Wones D.R. 1998. Nomenclature of the micas. *Canadian Mineralogist*, **36**(3):905-912.

Rio Doce Geologia e Mineração (Docegeo). 1988. Revisão litoestratigráfica da Província Mineral de Carajás. *In*: Congresso Brasileiro de Geologia, Belém, 35. *Anais...* p. 11-59.

Rodrigues D.D., Oliveira D.C., Macambira M.J.B. 2014. Geologia, geoquímica e geocronologia do Granito Mesoarqueano Boa Sorte, município de Água Azul do Norte, Pará – Província Carajás. *Boletim do Museu Paraense Emílio Goeldi. Série Ciências da Terra*, **9**(3):597-633. https://doi.org/10.46357/bcnaturais.v9i3.513

Santos J.O.S., Hartmann L.A., Faria M.S., Riker S.R., Souza M.M., Almeida M.E., Mcnaughton N.J. 2006. A compartimentação do Cráton Amazonas em províncias: avanços ocorridos no período de 2000-2006. *In*: Simpósio de Geologia da Amazônia, 9., 2006, Belém. *Anais...* Belém: SBG.

Santos P.A. 2013. *Geologia, Petrografia e Geoquímica da Associação Tonalito-Trondhjemito-Granodiorito (TTG) do extremo leste do Subdomínio de Transição, Província Carajás*. Dissertação de Mestrado, Programa de Pós-graduação em Geologia e Geoquímica, Instituto de Geociências, Universidade Federal do Pará, Belém, 68 p.

Santos P.A., Teixeira M.F.B., Dall'Agnol R., Guimarães F.V. 2013. Geologia, petrografia e geoquímica da associação tonalito-trondhjemito-granodiorito (TTG) do extremo leste do Subdomínio de Transição, Província Carajás - Pará. *Boletim do Museu Paraense Emilio Goeldi, Ciências Naturais*, **8**(3):257-290. https://doi.org/10.46357/bcnaturais.v8i3.551

Santos R.D., Galarza M.A., Oliveira D.C. 2013. Geologia, geoquímica e geocronologia do Diopsídio-Norito Pium, Província Carajás. *Boletim do Museu Paraense Emílio Goeldi, Ciências Naturais*, **8**(3):355-382. https://doi.org/10.46357/bcnaturais.v8i3.554

Santos R.F.S., Oliveira D.C., Silva F.F. 2018. Geocronologia U-Pb, classificação e aspectos evolutivos do Granito Marajoara, Província Carajás. *Geologia USP. Série Científica*, **18**(4):89-124. https://doi.org/10.11606/issn.2316-9095.v18-145323

Sardinha A.S., Barros C.E.M., Krymsky R. 2006. Geology, geochemistry, and U-Pb geochronology of the Archean (2.74 Ga) Serra do Rabo granite stocks, Carajás Province, northern Brazil. *Journal of South American Earth Sciences*, **20**(4):327-339. https://doi.org/10.1016/j.jsames.2005.11.001

Salazar-Naranjo A.F., Vlach S.R.F. 2018. On the crystallization conditions of the Neoproterozoic, high-K calc-alkaline, Bragança Paulista-type magmatism, southern Brasília Orogen, SE Brazil. *Brazilian Journal of Geology*, **48**(3):631-650. https://doi.org/10.1590/2317-4889201820180033

Scaillet B., Evans B.W. 1999. The 15 June 1991 eruption of Mount Pinatubo; I, Phase equilibria and pre-eruption P-T–fO2–fH2 conditions of the dacite magmas. *Journal of Petrology*, **40**(3):381-411.

Schumacher J.C. 1997. The estimation of ferric iron in electron micropobe analysis of amphiboles. *In*: Leake B.E. (Ed.). Nomenclature of Amphiboles. Report of the Subcommittee on Amphiboles of the International Mineralogical Association Commission on New Minerals and Mineral Names. *European Journal of Mineralogy*, **9**:623-651.

Silva A.C. 2012. *Geologia, petrografia e geoquímica dos granitóides arqueanos da área de Vila Jussara, Província Carajás*. Dissertação de Mestrado, Programa de Pós-Graduação em Geologia e Geoquímica, Instituto de Geociências, Universidade Federal do Pará, Belém.

Silva A.C., Dall'Agnol R., Guimarães F.V., Oliveira D.C. 2014. Geologia, petrografia e geoquímica de associações tonalíticas e trondhjemíticas arqueanas de Vila Jussara, Província Carajás, Pará. *Boletim do Museu Paraense Emílio Goeldi. Ciências Naturais*, **9**(1):13-45. https://doi.org/10.46357/bcnaturais.v9i1.536

Silva A.C., Oliveira D.C., Macambira M.J.B. 2010. Individualização e geocronologia de granitoides do Complexo Xingu, região de Vila Jussara, Município de Água Azul do Norte-PA, Província Mineral de Carajás. *In*: Congresso Brasileiro de Geologia, 45. *Anais*... Belém. CD-ROM.

Silva F.F., Oliveira D.C., Dall'Agnol R., Silva L.R., Cunha I.V. 2020. Lithological and structural controls on the emplacement of a Neoarchean plutonic complex in the Carajás Province, southeastern Amazonian, craton (Brazil). *Journal of South American Earth Sciences*, **102**:102696. https://doi.org/10.1016/j.jsames.2020.102696

Silva F.S., Oliveira D.C., Antonio P.Y., D'Agrella-Filho M., Lamarão C.N. 2016. Bimodal magmatism of the Tucumã area, Carajás Province: U-Pb geochronology, classification and processes. *Journal of South American Earth Sciences*, **72**:95-114. https://doi.org/10.1016/j.jsames.2016.07.016

Silva L.R., Oliveira D.C., Santos M.N.S. 2018. Diversity, origin and tectonic significance of the Mesoarchean granitoids of Ourilândia do Norte, Carajás province (Brazil). *Journal of South American Earth Sciences*, **82**:33-61. https://doi.org/10.1016/j.jsames.2017.12.004

Souza Z.S., Potrel H., Lafon J.M., Althoff F.J., Pimentel M.M., Dall'Agnol R., Oliveira C.G. 2001. Nd, Pb and Sr isotopes of the Identidade Belt, an Archaean greenstone belt of the Rio Maria region (Carajas province, Brazil): Implications for the Archaean geodynamic evolution of the Amazonian Craton. *Precambrian Research*, **109**(3-4):293-315. https://doi.org/10.1016/S0301-9268(01)00164-4

Tassinari C.C.G., Macambira M.J.B. 2004. A Evolução tectônica do Cráton Amazônico. *In*: Mantesso-Neto V., Bartorelli A., Carneiro C.D.R., Brito Neves B.B. (eds.). *Geologia do continente Sul-americano*: evolução da obra de Fernando Flávio Marques de Almeida. São Paulo.

Teixeira M.F.B. 2013. *Geologia, petrografia e geoquímica dos granitóides arqueanos da área de Sapucaia, Província Carajás*. Dissertação de Mestrado, Programa de Pós-graduação em Geologia e Geoquímica, Instituto de Geociências, Universidade Federal do Pará, Belém.

Teixeira M.F.B., Dall'Agnol R., Santos J.O.S., Kemp A., Evans N. 2019. Petrogenesis of the Paleoproterozoic (Orosirian) A-type granites of Carajás Province, Amazon Craton, Brazil: Combined in situ Hf-O isotopes of zircon. *Lithos*, **332-333**:1-22. https://doi.org/10.1016/j.lithos.2019.01.024

Teixeira M.F.B., Dall'Agnol R., Santos J.O.S., Oliveira D.C., Lamarão C.N., McNaughton N.J. 2018. Crystallization ages of Paleoproterozoic A-type granites of Carajás province, Amazon craton: Constraints from U-Pb geochronology of zircon and titanite. *Journal of South American Earth Sciences*, **88**:312-331. https://doi.org/10.1016/j.jsames.2018.08.020

Teixeira M.F.B., Dall'Agnol R., Santos J.O.S., Sousa L.A.M., Lafon J.M. 2017. Geochemistry, geochronology and Nd isotopes of the Gogó da Onça Granite: A new Paleoproterozoic A-type granite of Carajás Province, Brazil. *Journal of South American Earth Sciences*, **80**:47-65. https://doi.org/10.1016/j.jsames.2017.09.017

Teixeira M.F.B., Dall'Agnol R., Silva A.C., Santos P.A. 2013. Geologia, petrografia e geoquímica do Leucogranodiorito Pantanal e dos leucogranitos arqueanos da área a Norte de Sapucaia, Província Carajás, Pará: implicações petrogenéticas. *Boletim do Museu Paraense Emílio Goeldi. Ciências Naturais*, **8**(3):291-323. https://doi.org/10.46357/bcnaturais.v8i3.552

Topno A., Dey S., Liu Y., Zong K. 2018. Early Neoarchean A-type granitic magmatism by crustal reworking in Singhbhum craton: Evidence from Pala Lahara area, Orissa. *Journal of Earth System Science*, **127**(3):43. https://doi.org/10.1007/s12040-018-0947-y

Vasquez L.V., Rosa-Costa L.R., Silva C.G., Ricci P.F., Barbosa J.O., Klein E.L., Lopes E.S., Macambira E.B., Chaves C.L., Carvalho J.M., Oliveira J.G., Anjos G.C., Silva H.R. 2008. *Geologia e recursos minerais do estado do Pará*: Sistema de Informações Geográficas – SIG: texto explicativo dos mapas geológico e tectônico e de recursos minerais do estado do Pará. Pará, 328 p.

Whitney D.L., Evans B.W. 2010. Abbreviations for names of rock-forming minerals. *American Mineralogist*, **95**(1):185-187. https://doi.org/10.2138/am.2010.3371

Wones D. 1981. Mafic silicates as indicators of intensive variables in granitic magmas. *Mining Geology*, **31**(168):191-212. https://doi.org/10.11456/shigenchishitsu1951.31.191

Wones D., Eugster H. 1965. Stability of biotite: experiment theory and application. *American Mineralogist*, **50**(9):1228-1272.